Multiscalar model for the determination of spatially explicit riparian vegetation roughness

Rebecca Manners,[1] John Schmidt,[1,2] and Joseph M. Wheaton[1]

Received 16 August 2011; revised 4 November 2012; accepted 5 November 2012; published 27 January 2013.

[1] Improved understanding of the connection between riparian vegetation and channel change requires evaluating how fine-scale interactions among stems, water, and sediment affect larger scale flow and sediment transport fields. We propose a spatially explicit model that resolves patch-scale (submeter) patterns of hydraulic roughness over the reach scale caused by stands of shrubby riparian vegetation. We worked in tamarisk-dominated stands on the Yampa and Green Rivers in Dinosaur National Monument, northwestern Colorado, USA, where questions remain regarding the role of vegetation in inducing or exacerbating documented channel changes. Hydraulic roughness patterns were derived from patch-scale measurements made with detailed terrestrial laser scan (TLS) data that were extrapolated to reach scales based on correlation with light detection and ranging (LiDAR) (ALS) data. Two-dimensional, patch-scale, hydraulic models were used to parameterize the stage dependence of hydraulic roughness of typical patch types (i.e., sparse, moderate, and dense patches). We illustrate the value of using this approach to characterize vegetation roughness by applying our results to a two-dimensional hydraulic model of flow for one of our study sites. Results from this work predict that the roughness of vegetated floodplains increases with flow depth and is dependent on patch-scale stem organization. Geomorphically relevant patterns (i.e., areas of low or high shear stress that are likely to scour or fill during high flows) become apparent with the detail introduced by spatially explicit, depth-dependent roughness. To our knowledge, the multiscalar analysis presented here is the first to mechanistically account for shrubby riparian vegetation stand structure, and associated hydraulic roughness of vegetation patches, at the reach scale.

Citation: Manners, R., J. Schmidt, and J. M. Wheaton (2013), Multiscalar model for the determination of spatially explicit riparian vegetation roughness, *J. Geophys. Res. Earth Surf.*, *118*, 65–83, doi:10.1029/2011JF002188.

1. Introduction

[2] Riparian vegetation encroachment onto active alluvial surfaces can significantly modify channel form, resulting in narrowing and simplification of planform [*Tal and Paola*, 2007; *Corenblit et al*., 2009]. An improved understanding of the processes that link vegetation and geomorphic form is especially important in light of major shifts in riparian communities caused by water development [*Rood and Mahoney*, 1990; *Auble et al*., 1994; *Merritt and Wohl*, 2006], climate change [*Meyer et al*., 1999; *Gibson et al*., 2005], and the invasion of non-native species [*Friedman et al*., 2005].

[3] At a fundamental level, vegetation-induced channel change results from the interaction of stems, stream flow, and transported sediment [*Schnauder and Moggridge*, 2009]. Stems perturb the flow field, modifying the distribution of velocity and shear stress, and, as a result, patterns of sediment entrainment and transport [*Nepf et al*., 1997; *Bennett et al*., 2002; *Zong and Nepf*, 2010]. Over time, these patterns may cause net erosion and deposition, which are the mechanisms that alter the channel cross section and/or planform.

[4] Although the processes that cause channel narrowing occur at small spatial scales, the geomorphic implications of these processes are typically observed and investigated at larger spatial scales, such as that of a reach (10–20 channel widths). There has been limited progress in applying the insights gained from stem-scale studies to the reach-scale changes that are of geomorphic significance [*Forzieri et al*., 2012]. One approach to applying small-scale insights to larger scale processes involves development of techniques and classification schemes that empirically link coarsely measured vegetation attributes, such as vegetation height [*Cobby et al*., 2001; *Mason et al*., 2003], crown characteristics [*Antonarakis et al*., 2008; *Forzieri et al*., 2011], species [*Stoesser et al*., 2003], or vegetation "type" (i.e., shrub versus grass, flexible versus rigid) [*Darby*, 1999; *Brookes et al*., 2000], to the hydraulic resistance of vegetation. Application of these techniques and classification schemes requires assumptions about

[1]Intermountain Center for River Rehabilitation and Restoration, Department of Watershed Sciences, Utah State University, Logan, Utah, USA.
[2]Now at Grand Canyon Monitoring and Research Center, US Geological Survey, Flagstaff, Arizona, USA.

Corresponding author: R. Manners, Intermountain Center for River Rehabilitation and Restoration, Department of Watershed Sciences, Utah State University, 5210 Old Main Hill, NR 210, Logan, UT 84322, USA. (Rebecca.Manners@usu.edu)

2169-9003/13/2011JF002188

stand structure, either applied as typical attributes [e.g., *Griffin et al*., 2005], or through inferred relationships linked to a single variable (i.e., vegetation height) [e.g., *Mason et al*., 2003]. However, riparian vegetation communities often have species assemblages and stand ages that result in variable stand structure. In these cases, techniques based on coarsely measured variables oversimplify the hydraulic effects of vegetation. Additionally, many riparian corridors are dominated by shrubby species [*Friedman et al*., 2005] whose stand structure is complex and cannot be characterized based on canopy structure.

[5] The ability to control environmental conditions in a laboratory setting has resulted in improved methods to quantify the stem-scale impact of vegetation on the flow field. Such approaches are capable of accounting for specific attributes of vegetation structure, including stem density, stem spacing, flexibility, and relative submergence [*Petryk and Bosmajian*, 1975; *Bennett et al*., 2002; *Jarvela*, 2004; *Liu et al*., 2008]. These physically meaningful results are limited in spatial extent, suffer from issues of how to apply the results to larger scales, and are generally restricted to idealizations of vegetation, rather than actual plants. Little progress has yet been made on how to apply the ever-improving insights gained from small-scale studies in laboratories to the field scale.

[6] In this study, we linked detailed measurements of stand structure derived from terrestrial laser scanning (TLS; also called ground-based LiDAR) to reach-scale riparian vegetation patterns derived from airborne LiDAR (also referred to as airborne laser scanning [ALS]). Acknowledging that fine-scale interactions among stems, water, and sediment may be critical in the accurate identification of the role of riparian vegetation, we developed a method that merges small-scale, high-resolution TLS data and broader extent ALS data. We related TLS data collected at the patch scale (10^0–10^1 m) to the reach scale (10^2–10^3 m) using a scaling methodology. This methodology does not necessitate a "brute force" approach whereby high-resolution TLS data are collected for an entire reach. Our method is inspired by the fact that TLS is not practical to deploy over large areas or in thick vegetation. We describe a methodology to extrapolate detailed TLS data to the reach scale. We quantify the patch-scale stand structure of shrubby riparian vegetation using TLS data; relate physically based, depth-dependent roughness to stand structure; upscale these relationships from patch scale to reach scale using ALS data; and describe the response of reach-scale flow hydraulics to the patch-scale distribution and structure of riparian vegetation. We conclude by discussing the implications of riparian vegetation invasion on channel hydraulics by using our method to model the bed shear stress distribution in the absence and presence of riparian vegetation. Although we present only limited field verification of our model, the methodology described here represents a novel effort to account for variable stand structure and its effects on reach-scale hydraulics.

2. Tamarisk in the Colorado River Basin

[7] We focused on the invasive non-native riparian shrub tamarisk (*Tamarix* spp.). During the past century, tamarisk has densely colonized alluvial valleys of most of the Colorado River system. A general trend in these valleys has been toward denser vegetation encroaching along the margins of the active channel and greater dominance by tamarisk and native willow species (*Salix* spp.). A decline of bare, dynamic sand bars has generally led to the simplification of channel planform [*Turner and Karpiscak*, 1980; *Webb et al*., 2007].

[8] Tamarisk's spread through the basin was concurrent with other environmental shifts, including the closure of large dams and 20th century climate change [*Graf*, 1978; *Allred and Schmidt*, 1999; *Birken and Cooper*, 2006]. As a response to the changes in these environmental drivers, channel narrowing has been ubiquitous [e.g., *Hereford*, 1984; *Grams and Schmidt*, 2002]. There is extensive documentation of channel narrowing by inset floodplain formation in many parts of the Colorado River basin [e.g., *Graf*, 1978; *Hereford*, 1984; *Grams and Schmidt*, 2002]. These studies implicate either of two causes of narrowing. One potential cause is the invasion of riparian vegetation that results in increased bank stabilization and roughness that induces sediment deposition [*Graf*, 1978; *Birken and Cooper*, 2006; *Dean and Schmidt*, 2011]. The other potential cause is decreased flood flows due to water development. Decreased flows may result in sediment mass balance surplus, leading to the development of inset floodplains, regardless of whether or not invasive riparian vegetation is present [*Everitt*, 1993; *Allred and Schmidt*, 1999]. Improved understanding of the mechanisms by which riparian vegetation affects the local hydraulics through tamarisk stands and, in turn, larger scale flow patterns is essential for understanding the relative role of these two causes of narrowing [*Schnauder and Moggridge*, 2009].

3. Study Area

[9] Our study involved two sites in Dinosaur National Monument (Figure 1), located in the middle Rocky Mountains in eastern Utah and western Colorado: Laddie Park in Yampa Canyon on the Yampa River, and Seacliff in Whirlpool Canyon on the middle Green River downstream from the Yampa. The channels at both of these sites have progressively narrowed during the 20th century [*Grams and Schmidt*, 2002]. The oldest surviving tamarisk individual recovered to date in this area germinated in 1938 [*Cooper et al*., 2003]. We analyzed extensive geomorphic, hydrologic, and vegetative data obtained from ongoing data collection efforts at the two sites [*Manners et al*., 2011]. Additionally, ALS data were obtained from a flight over the study sites in October 2008, and three-band multispectral imagery was obtained from a flight in June 2010.

[10] The two study sites are both 0.6 km long (Figure 2). Laddie Park is in the downstream part of Yampa Canyon where the Yampa River has established a series of incised meanders. The average channel slope is 0.0009, and the average channel width is 106 m [*Larson*, 2004]. In contrast, the Green River in Whirlpool Canyon has a steeper slope (0.002) and narrower channel width (64 m) [*Grams and Schmidt*, 2002]. Whirlpool Canyon is affected by debris fans. In such a canyon, fan-eddy complexes occur wherever debris fans partly constrict the channel, thereby creating backwaters upstream from the debris fan and lateral separation eddies and expansion gravel bars downstream [*Schmidt and Rubin*, 1995]. The flow regime of the Yampa River is relatively unregulated, but the flow regime of the middle Green River reflects the combined influences of the Yampa

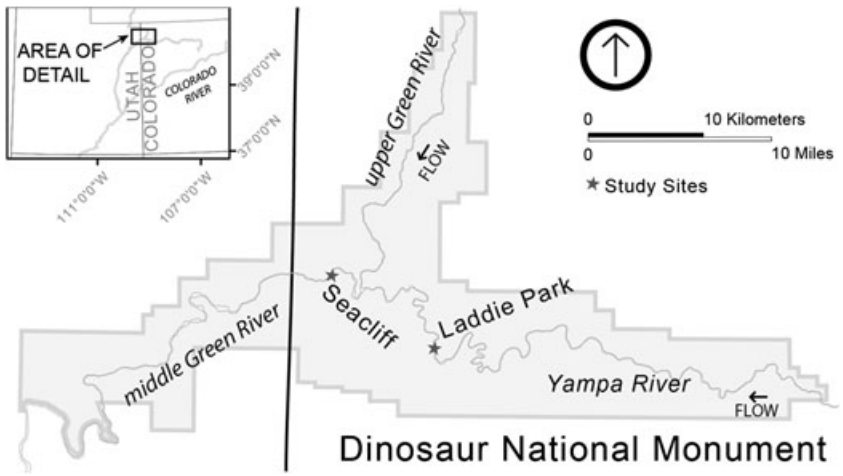

Figure 1. Study areas in Dinosaur National Monument, Colorado.

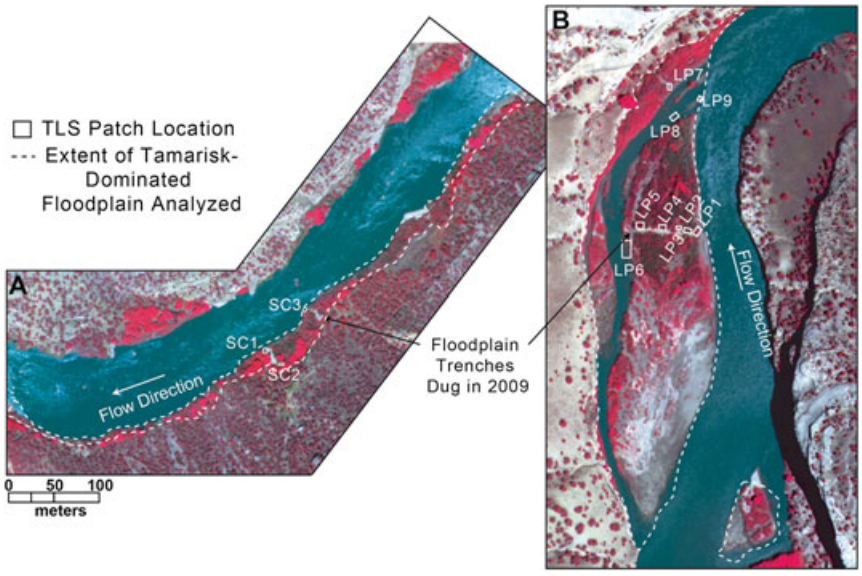

Figure 2. Twelve vegetation patches captured with the terrestrial laser scanner. These patches are located at two study sites, (A) Laddie Park on the Yampa River and (B) Seacliff on the Green River. Dashed lines delineate tamarisk-dominated floodplain areas where the multiscalar model was applied.

River and the flow regulation by Flaming Gorge Dam on the upper Green River [*Grams and Schmidt*, 2002].

[11] Laddie Park is in a relatively wide part of Yampa Canyon where there are discontinuous floodplains, an island that splits the channel, and mid-channel bars. Laddie Park is upstream from a pronounced bedrock bend in the river whose radius of curvature is small. At flood stage, flow is backwatered upstream from this bend. The island and parts of the floodplain in Laddie Park have been progressively colonized during the past 70 years with tamarisk, sandbar willow (*Salix exigua*), and,to a lesser extent, box elder (*Acer negundo*). Today, the woody riparian vegetation community of the Laddie Park reach is 86% tamarisk, 11% sandbar willow, and 3% box elder.

[12] The Seacliff site consists of a series of small debris fans and eddy bars on river left. We focus on the eddy bars that have been progressively colonized by tamarisk during the past 60 years. Today, the woody riparian vegetation community of these bars in the Seacliff reach is composed of 62% tamarisk and 38% box elder.

4. Characterization of Patch-Scale Stand Structure and Depth-Dependent Roughness

[13] Extrapolation of the results of small-scale processes to large areas can be accomplished in a spatially explicit manner by appropriate parameterization. For example, *Hodge et al*. [2007] used a discrete element model of the entrainment and transport of individual grains at the patch scale to develop basic transport relations, which were upscaled and used to parameterize a much broader reach-scale, reduced complexity, morphodynamic model. In the case of scaling roughness caused by vegetation, parameterization must account for the differences in growth and

distribution of riparian vegetation that cause complex and highly variable interactions among individual plants. Therefore, spatially explicit characterization of vegetation's role in perturbing the flow field should account for the patterns of riparian vegetation growth and density and how these characteristics change with height above the ground surface.

[14] Our multiscalar analysis began at the patch scale. We defined a patch to be a cluster of similarly sized, spaced, and aged individual plants with similar stand structure (i.e., height, dominant stem size, stem spacing). High-density TLS point clouds (i.e., >200 pts/m^2) were used to characterize the patch-scale stand structure, which we defined as the height-dependent stem density and vertical projected area. We used the detailed TLS data to parameterize the patch-scale roughness.

4.1. Methodology: Deriving Stand Structure From Terrestrial Laser Scan Data

4.1.1. TLS Data Collection

[15] We positioned a Leica Scan Station 2 upstream from 12 patches to acquire a high-resolution (0.005 m point spacing) point cloud (Figure 3 and Table 1). Data were acquired in July 2010 during base flows when the patches were not inundated. The ground topography of each patch was relatively flat. Tree ages, as determined by the germination year of a sample of tamarisk stems within or close to a patch, ranged between 10 and 60 years. The substrate in these patches was either sand or gravel. Individual plants in some patches had been buried after germination by as much as 3.5 m of sand and mud, as observed in floodplain trenches [*Manners et al.*, 2011]. The bed-parallel area of each patch varied between 10^1 and 10^2 m^2; patches with denser vegetation were of smaller size.

[16] In the field, the scanner was positioned to collect data from the perspective of the predominant direction of overbank flows. One scan per patch was collected. We assumed that the flow direction on the floodplain is approximately the same at all flows. Thus our single-scan perspective was a reasonable characterization of how vegetation interacts with the flow. We also assumed that the maximum streamwise patch length of 3–9 m prevented significant occlusion, or shadowing, of stems because TLS measurements are line of sight [*Warmink*, 2007]. We occupied several control points throughout the two field sites in order to register the scans to each other and convert scan data to universal transverse mercator (UTM) coordinates. Each scanner setup lasted

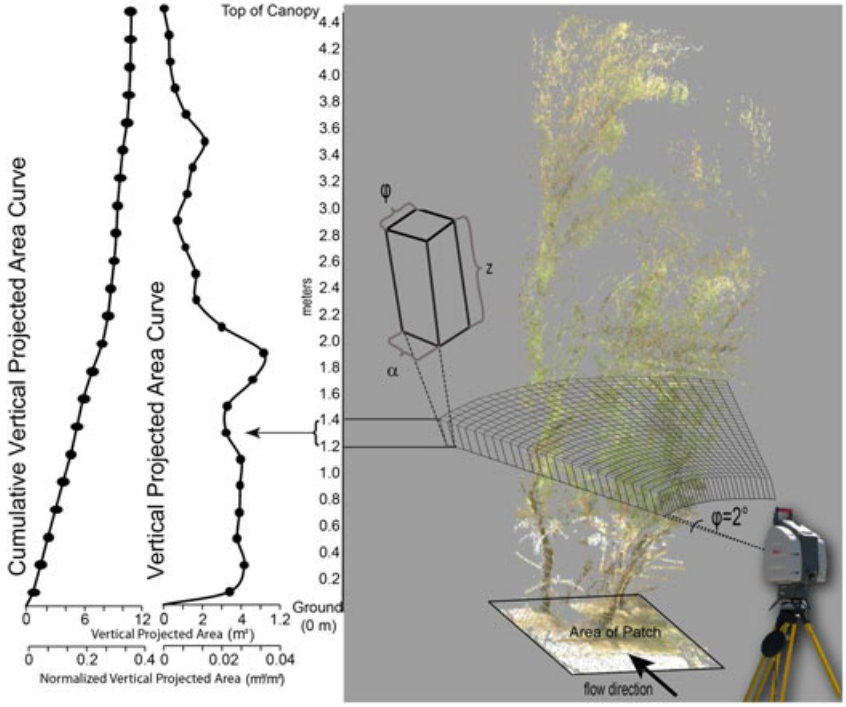

Figure 3. Schematic of the procedure used to quantify vertical projected area profiles from a three-dimensional point cloud. We established a cylindrical polar grid, composed of three-dimensional cells or voxels, for each patch centered on the scanner location. Each cell's vertical height (z) was 0.20 m. The depth along the radial distance from the scanner (α) was 0.10 m. The third dimension was defined by the angular distance (ϕ) that was set to 2°. Thus, the length of this dimension varied based on the distance of the cell to the scanner along the plane defined by αϕ. For illustrative purposes, we only show a single 0.20-m horizontal slice, composed of grid cells all located at the same height above the ground surface. Vertical projected area ($A_{P,vert}$) was first calculated within each cell and then summed over the patch at each 0.20-m interval. Patch-total $A_{P,vert}$ values were normalized by the bed-parallel area of the patch, resulting in normalized vertical projected area values ($A_{P,vert(n)}$). We use two types of curves from this analysis: a vertical projected area curve that is representative of the vertical distribution of stems through the profile, and the cumulative vertical projected area curve that represents the sum of all stems through the profile and is closer to what the flow field encounters.

Table 1. Attributes of the 12 Tamarisk Patches Whose Stand Structure Was Characterized by Terrestrial Laser Scans

	Patch[a]	Patch Size (m^2)	Age (years)	Substrate[c]	Depositional History[d] (cm)	Profile Group
1	LP1	28.9	20	s	160	moderate
2	LP2	18.7	55-60	s	190	dense
3	LP3	10.3	50-55	s	85	dense
4	LP4	21.2	60	s	125	moderate
5	LP5	29.2	45	s	300	moderate
6	LP6	136.5	20	g	0	sparse
7	LP7	11.9	<10	s	50	moderate
8	LP8	37	20	g	0	sparse
9	LP9	9.8	20	g	0	sparse
10	SC1	12.8	15	s	110	dense
11	SC2	6.5	50	s	140	dense
12	SC3	9.8	15	s	35	dense

[a]LP denotes patches located at the Laddie Park study site on the Yampa River, and SC denotes patches located at the Seacliff site on the Green River

[b]Age was determined by identification of the germination year of a sample of tamarisk located either within or close to each patch.

[c]s=sand and g=gravel

[d]Depositional history refers to the amount of fine sediment that has been deposited around those individuals recovered for aging. We measured the amount of deposition as the total accumulation of sediment above the germination point.

between 1 and 4 hours and acquired a total of 10^5–10^7 points per patch.

4.1.2. Scan Data Analyses

[17] We calculated the stand structure of different horizontal slices of the patch above the ground surface using the method of *Straatsma et al*. [2008]. A series of models and Python scripts were created in ESRI's ArcGIS ModelBuilder to convert raw point cloud data into metrics, such as vegetation density and vertical projected area. While the majority of vegetation studies using TLS data have quantified vegetation density by identifying individual stems [e.g., *Thies et al*., 2004], *Straatsma et al*. [2008] adopted *MacArthur and Horn's* [1969] gap fraction method and quantified vegetation density as the ratio of laser pulses emitted to those not intercepted. Such a methodology treats TLS returns as a proxy for density, which is appropriate for tamarisk and other shrubby riparian species with complicated branching patterns (Figure 4).

[18] We created a grid of three-dimensional cells, or voxels, based on a cylindrical polar coordinate system in ArcGIS (Figure 3). The vertical height of each cell (z) was 0.20 m; thus, the grid was composed of a series of 0.20-m-thick adjoining layers that spanned the vertical distance from the ground surface to the top of the tamarisk stand. The depth of each voxel along the radial distance from the scanner (α) was 0.10 m. Therefore, the number of voxels in the radius from the scanner depended on the depth to which the laser pulses penetrated the patch, as explained below. The third dimension of each voxel, the angular distance (φ), was held constant at 2°. Thus, the length of this dimension varied based on the distance of the cell to the scanner–parallel plane defined by αϕ. After manually removing ground points in Leica's Cyclone Software, we then used this polar cylindrical grid to quantify vegetation density (D_v) from the point cloud. For each grid cell, vegetation density, $D_{v,ij}$. was approximated as:

$$D_{v,ij} = \frac{1}{a}\ln\left(\frac{T_{ij}-B_{ij}}{T_{ij}-B_{ij}-G_{ij}}\right) \quad (1)$$

Figure 4. Example of a patch of *Tamarix* spp. (tamarisk) at Laddie Park. Flow is from left to right in photo.

where T_{ij} is the total number of emitted laser pulses that would have passed through the distal boundary of the cell if no obstructions were present, B_{ij} is the number of pulses intercepted between the scanner and the cell, and G_{ij} is the number of points intercepted within the cell. As vegetation density is defined as the vertical projected area per unit volume, the vertical projected area of the stems in the cell, $A_{P,vert,ij}$ (m^2), was then calculated as:

$$A_{P,vert,ij} = D_{v,ij} \times A_{ij} \times 0.2 \quad (2)$$

where A_{ij} is the basal area of the individual voxel parallel the plane defined by αϕ. Vertical projected area ($A_{P,vert}$), defined as the area of the vegetation projected normal to the flow, was summed over the patch to get a single value of $A_{P,vert}$ for each 0.20-m horizontal slice. We divided $A_{P,vert}$ by the bed-parallel basal area of a given patch (A) to get a normalized vertical projected area ($A_{P,vert(n)}$) to account for the variability in patch size. Both vertical projected area and cumulative vertical projected area curves were obtained by this method and used to evaluate the structure of tamarisk stands (Figure 3).

4.2. Methodology: Quantification of Stage-Dependent Roughness

[19] We created two-dimensional hydraulic models of flow in each patch to link stand structure to the patch's hydraulic roughness (Figure 5). Scan data were converted into two-dimensional stem maps that described the vertical projected area and spatial organization of each patch. These maps used the cumulative $A_{P,vert}$ value for each voxel to define the size and position of vertical cylinders. Due to the vertical averaging implicit in a two-dimensional representation of vegetation, we created a unique stem map for each 0.20-m-thick increment to depict the vertically changing spatial configuration of the cumulative $A_{P,vert}$. In reality, not all stems line up with the voxels. A clustering of high $A_{P,vert}$ voxels is likely a product of a stem whose diameter exceeds the angular distance of the voxel (Figure 3). We accounted for this by merging adjacent cylinders that intersect. This new merged cylinder was then moved along the αϕ plane so that its center

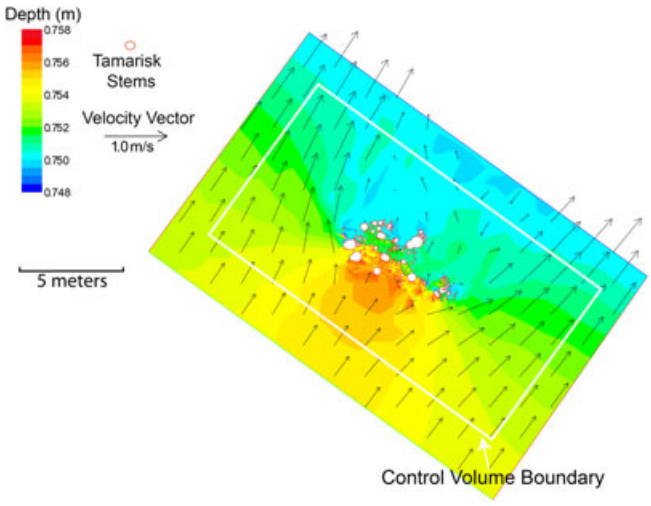

Figure 5. Example of a single two-dimensional patch model run for patch LP2. "Tamarisk stems" depicted here are a series of vertical cylinders (red circles) representative of the cumulative vertical projected area and spatial organization of a patch at a given height. The River2D depth (contours) and velocity (vectors) solutions are shown. See text for further explanation of the modeling procedures.

matched the center of those voxels used to define it (Figure 5). We acknowledge that vertical, cylindrically shaped "stems" are an oversimplification of the complex three-dimensional branching pattern.

[20] We used River2D to develop the stem map mesh and run the various flow scenarios. We chose River2D as it uses a triangular unstructured networks (TIN)-based unstructured mesh, which is suitable for varying the resolution to adequately capture the two-dimensional stem maps. River2D uses a finite element method to solve the basic equations of vertically averaged two-dimensional flow [*Steffler and Blackburn*, 2002]. Mass and momentum are conserved in the two horizontal dimensions, solving for bed and bank shear stresses with the Manning equation and a Bousinessq-type eddy viscosity, respectively. Because the fundamental goal of the two-dimensional patch model was to resolve the flow field through individual "stems," we assigned high node spacing at the edges of the stems (0.0003–0.0004 m), represented as no-flow boundaries. Elsewhere, node densities were relaxed. *Steffler and Blackburn* [2002] suggest that a minimum of four nodes along an obstruction in each of the four horizontal directions (i.e., positive and negative streamwise direction and positive and negative cross-stream direction) are necessary to reliably resolve a feature in the flow field. Thus, in the coarsest sense, our meshes accounted for stems with 0.001-m diameters, while the majority of the stems in our stem maps had diameters greater than 0.005 m. This is important as it means the computational mesh can be constructed to allow us to adequately represent the impact of the obstructions on the flow field and back out the effective drag from the solution.

[21] The model domain extended beyond the defined patch to ensure unobstructed flow conditions in the upstream and lateral directions (Figure 5). Node spacing through the patch, outside of the stems, was set to 1 m. A unique numerical mesh was created for each stem map. We created meshes with the intent of making depth-averaged predictions from the bed, for 0.20-m flow depth increments, to evaluate changes in roughness and hydraulics. To ensure that flow depth within the patch was less than the upper boundary of the 0.20-m increment, we assigned the flow depth at the downstream boundary as 0.05 m less than the upper boundary of the cumulative $A_{P,vert}$ profile. For example, for a stem map created for the cumulative $A_{P,vert}$ profile whose upper limit was 0.80 m above the bed, the assigned downstream flow depth was 0.75 m.

[22] Each mesh was assigned a bed roughness height (k_s) consistent with the dominant bed material type for a given patch; gravel (k_s=0.4 m) or sand (k_s=0.1 m). Bed roughness heights were assumed constant for all flow depths within a given patch [*Whiting and Dietrich*, 1990]. In order to simplify our approach and focus on vegetative roughness, we did not account for bed form roughness, although we recognize that parts of the bed surface in the patches could support ripples at some flows. We converted bed roughness height into roughness coefficients (Manning's n), in order to solve for total patch roughness (see below), and thus, bed roughness became depth-dependent based on the following equation:

$$n = \frac{y^{1/6}}{2.5\sqrt{g}\,ln\left(\frac{12y}{k_s}\right)} \tag{3}$$

where g is the acceleration from gravity and y is flow depth.

[23] Flow rates for individual model runs were chosen so as to maintain constant water surface slope (~0.001) through the patches. All flows filled the extent of the model domain, and thus, the model did not need to account for the wetting and drying of elements. Results were iteratively solved for depth and velocity at each node by River2D until the model reached a steady state.

[24] Total patch roughness, n_{patch}, was partitioned into roughness caused by the bed, n_{bed}, and roughness caused by vegetation, $n_{vegetation}$, based on

$$n_{patch} = n_{bed} + n_{vegetation} \tag{4}$$

where bed roughness was derived from the bed roughness height (k_s) specified for each patch type. For vegetation roughness, we adopted an approach first proposed by *Petryk and Bosmajian* [1975] and subsequently used by many researchers [e.g., *Fathi-Maghadam and Kouwen*, 1997; *Jarvela*, 2004; *Musleh and Cruise*, 2006] that relates a roughness coefficient to the energy extracted by vegetative elements

$$n_{vegetation} = \sqrt{4C_D\left(A_{P,vert}/A\right)\frac{y^{1/3}}{8g}} \tag{5}$$

where C_D is the vegetative drag coefficient, $A_{P,vert}$ is the cumulative vertical projected area of the vegetation, and A is the bed-parallel, basal area of the patch. While C_D values may be derived from the literature [e.g., *Nepf*, 1999], our goal was to link the specific stand structure of tamarisk patches to their effects on channel hydraulics. Consequently, we back-calculated C_D for each two-dimensional patch model from the drag force equation

$$F_{D,veg} = \frac{1}{2}\rho C_D U_r^2 A_{P,vert} \tag{6}$$

where $F_{D,veg}$ is the bulk-streamwise drag force on the stems, ρ is the density of water, and U_r is the upstream reference velocity taken as the average velocity across the upstream boundary of the control volume.

[25] To quantify $F_{D,veg}$, we calculated the momentum extracted through the control volume surrounding each patch (Figure 5) [*Shields and Gippel*, 1995; *Manners et al.*, 2007]. The lateral boundaries of the control volume were delineated based on the extent of the patch-influenced flow field defined as the transition from flow vectors with a cross-stream component to those with no cross-stream component. We consistently defined the boundaries in this manner and did not evaluate the sensitivity of the drag calculation as a result of the location of the control volume boundary. The net external force on a system ($F_{external}$) is equal to the change of momentum through the control volume ($F_{downstream}$ - $F_{upstream}$)

$$F_{external} = F_{downstream} - F_{upstream} \tag{7}$$

[26] Assuming steady flow and defining the two external forces within each patch model that change the momentum through the system as the shear stress exerted by the bed (F_{bed}) and the forces exerted by the stems ($F_{D,veg}$), we relate these external forces to the forces across the upstream and downstream control volume boundary

$$F_{D,veg} + F_{bed} = \left(F_{static} + F_{dynamic}\right)_{downstream} - \left(F_{static} + F_{downstream}\right)_{upstream} \tag{8}$$

where F_{static} is a pressure force that is equal to the hydrostatic pressure, p, of the water normal to flow,

$$F_{static} = \int p dA_{vert} \tag{9}$$

and $F_{dynamic}$ is the momentum flux across the control volume boundary (either upstream or downstream),

$$F_{dynamic} = \int \rho U^2 dA_{vert}. \tag{10}$$

[27] In equations (9) and (10), U is the depth-averaged velocity at a point across the boundary, and A_{vert} is the area vector that has the magnitude of the area and is directed normal to the control volume boundary in question. The force exerted by the bed is defined as

$$F_{bed} = \int \tau_b dA \tag{11}$$

where τ_b is the near bed shear stress obtained as model output, and A is the area parallel to the bed within the control volume. Rearranging equation (8) to solve for the bulk, streamwise force on the stems, and substituting equations (9)–(11),

$$F_{D,veg} = \left(F_{static} + F_{dynamic}\right)_{downstream} - \left(F_{static} + F_{dynamic}\right)_{upstream} - F_{bed} = \left[\int \left(p + \rho U^2\right) dA_{vert}\right]_{downstream} - \left[\int \left(p + \rho U^2\right) dA_{vert}\right]_{upstream} - \int \tau_b dA \tag{12}$$

[28] We also accounted for stem flexibility of tamarisk patches as the patches become submerged. As flows increase, the force of the water on the stems pushes the stems downstream, and the effective stem height (i.e., the height interacting with the flow in the vertical) decreases. We took a simplified approach to quantifying the deflected height of stems. With a known U and C_D, we adopted a version of the beam elasticity equation applied to the midpoint of the stems to quantify the deflection of a single representative stem [*Kubrak et al.*, 2008; *Velasco et al.*, 2008], or displacement of the stem axis in the water flow direction $\delta(x)$,

$$\delta(x) = \frac{{}^1\!/_2 \rho C_D U^2 d}{EI} \tag{13}$$

where d is the average stem diameter, E is the stiffness modulus of which a constant value experimentally determined for tamarisk of 13.1×10^8 N/m^2 was used [*Freeman et al.*, 2000], and I is the cross-area inertial modulus calculated from the average stem diameter. In equation (13), the numerator represents the force, or hydrodynamic thrust, on the midpoint of the modeled stem, and the denominator is a mechanical property of the stem.

[29] To account for submergence and deflection, we decreased $A_{P,vert}/A$ in equation (5) based on the ratio of the flow depth that interacts with the vegetation to the portion of flow depth that does not. For example, based on the elasticity of a typical tamarisk stem, a flow depth of 2.4 m interacting with a 2.2-m-tall patch of tamarisk deflects the midpoint of the average stem in the streamwise direction ($\delta(x)$) by 0.09 m, thereby reducing the effective height (i.e., the total amount of the flow column interacting with the stem) to 2.07 m. Thus, 0.33 m (or 8%) of the water profile is not directly obstructed by the vegetation. $A_{P,vert}/A$ was reduced by 8%, and equation (5) was then solved for the new vegetation roughness value.

[30] We acknowledge that this approach has limitations. Bending of stems in the flow and the submergence of vegetation is fundamentally a three-dimensional problem [*Stephan and Gutknecht*, 2002]. By using a depth-averaged velocity, we likely underestimate velocities, and, as a result, the degree of stem deflection. Additionally, we do not update C_D values in equation (6), which were calculated for stiff stems. This simplification, along with our representation of complex tamarisk patches as single stems by using the patch-average stem diameter in equation (13), introduces uncertainty.

4.3. Results: Vegetation Profiles and Hydraulic Influence

[31] The 12 cumulative, normalized, vertical projected area ($A_{P,vert(n)}$) profiles of the tamarisk-dominated patches were classified into three groups (Figure 6). An analysis of variance among the three groups indicates that their $A_{P,vert(n)}$ values are statistically different ($P < 0.001$). Relatively young (<20 years old) patches whose stand height was short (<3 m) made up one group (Table 1). Hereafter, we refer to this group of patches as the "sparse group." These patches occur on low-elevation gravel bars that are inundated by common floods. This hydraulically stressful environment presumably causes the short stature and sparse plant density. Cumulative $A_{P,vert(n)}$ values for this group range from a minimum of 0.01 to 0.18 m^2/m^2. Patches of the other two groups grow in fine sediment. Maximum height of these patches was similar and ranged between 3.0 and 5.9 m and in age from <10 to 60 years old (Figure 6). One of this group's cumulative

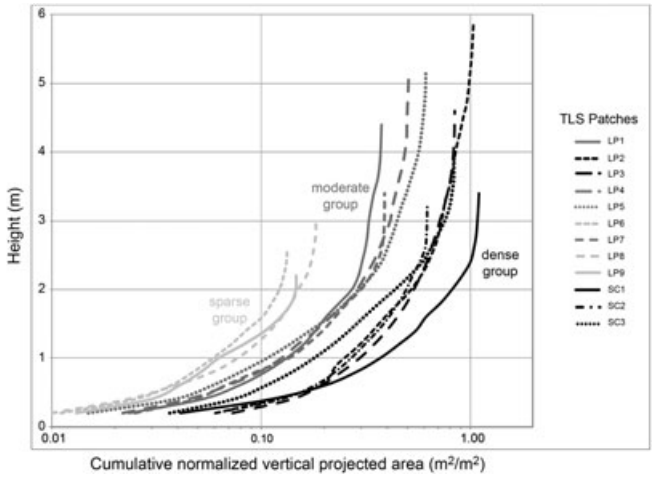

Figure 6. Cumulative normalized vertical projected area ($A_{P,vert(n)}$) curves for the 12 patches, classified into three vegetation density groups: sparse, moderate, and dense.

$A_{P,vert(n)}$ values ranged between 0.03 and 0.61 m^2/m^2, and we refer to these patches as the "moderate group." The other group's cumulative $A_{P,vert(n)}$ values ranged between 0.07 and 1.10 m^2/m^2, and we refer to these patches as the "dense group." We used this profile classification scheme to extrapolate the characteristics of tamarisk to the reach scale.

[32] Drag coefficients calculated for hydraulic model runs for each patch and for different stages ranged from 0.1 to 1.9. We used an analysis of variance to evaluate differences in C_D among the three vertical projected area profile groups (sparse, moderate, dense). For flow depths of 1 m and less, C_D was not statistically different among the three groups (mean=1.0, sd=0.3). However, C_D was different among groups for flow depths greater than 1 m ($P<0.001$). Drag coefficients were greatest for the dense patches (mean=1.5, sd=0.2) and smallest for moderate patches (mean=1.1, sd=0.1); sparse patches had intermediate values (mean=1.3, sd=0.1). We explore the potential cause of the observed trend in C_D values for the different density patches in section 6.1.

[33] Patch roughness caused by flow through vegetation generally increases with increasing flow depth to the point where the vegetation is completely submerged; thereafter, roughness decreases (Figure 7). Roughness increases with depth because cumulative vertical projected area also increases with depth. However, the relationship between projected area and roughness is not linear. This is especially apparent for flow depths less than 1.2 m. As expected, we find that $A_{p,vert(n)}$ for the moderate group is greater than for the sparse group. However, the vegetation and total patch roughness for the sparse group are slightly greater than those for the moderate group (Figure 7). We attribute some of the greater patch roughness values of the sparse group at low flows to the gravel substrate. For flow depths less than 0.6 m in the sparse group patches, the bed contributes greater roughness than do the stems (Figure 7). However, this difference may also be attributed to a slightly higher C_D value in the sparse group than in the moderate group.

[34] Where flow depth exceeds 1.2 m, roughness values for moderate density patches increase at a greater rate than do the values for sparse patches. A maximum n value of 0.178 occurs at flow depths between 2.8 and 3.0 m in moderate patches. Sparse patches become fully submerged when the local flow depth exceeds 2.2 m. From 2.2 to 3.0 m, the vegetation roughness of sparse patches decreases from 0.106 to 0.099. Stage-dependent vegetation roughness values are greatest for dense patches and range from 0.045 at a flow depth of 0.20 m to 0.293 at a flow depth of 3.0 m.

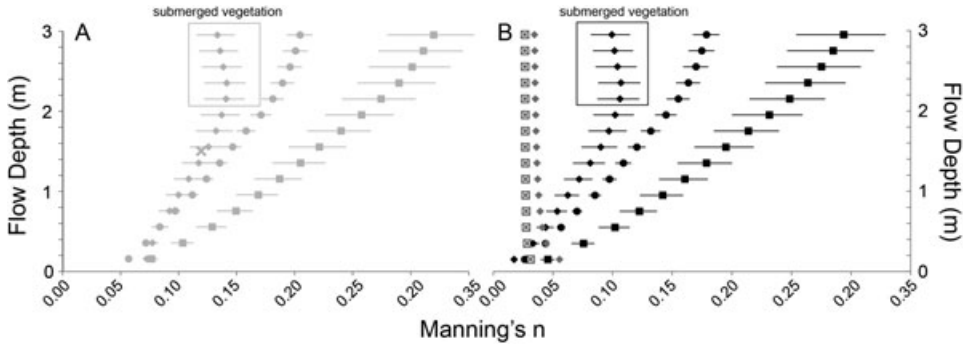

Figure 7. Average roughness profiles for the three vegetation density groups. (A) Total patch roughness ($n_{patch}=n_{veg}+n_{bed}$) for the dense group (squares), moderate group (circles), and sparse group (diamonds). (B) Profiles of n_{veg} (black) and n_{bed} (gray) for the three groups. The moderate and dense groups have the same n_{bed} values. Total patch roughness, vegetation roughness, and bed roughness are shown separately to illustrate the significant contribution of vegetation to total roughness. $A_{P,vert}/A$ data (same value as $A_{P,vert(n)}$) used to quantify n_{veg} (from equations (5) and (14)) are averages of all patches within that group. Error bars were calculated from standard deviation of back-calculated C_D values from two-dimensional patch models. In general, vegetation roughness and total patch roughness increase with increasing depth. The exception is the sparse group. When the sparse group is overtopped at a flow depth of 2.4 m, roughness begins to decrease. The "x" shown in Figure 7A is a data point taken from the experimental work of Freeman et al. [2000] and shows good agreement with our results.

5. Upscaling From the Patch Scale

5.1. Methodology

[35] Patch-scale data are insufficient to describe reach-scale riparian vegetation patterns, because patch data alone do not inform how those data can be extrapolated to the reach scale. We took advantage of the overlap in coverage of TLS and ALS data in the study areas to extrapolate patch-scale field measurements to the reach scale by creating a relation between stand structure and the corresponding hydraulic roughness. Thus, we leveraged the precision of the detailed TLS data against the spatially extensive, yet coarser, ALS data set. First, we created a model that related ALS to TLS data using the 12 patches and then extended this model to the entire study area. While the scales over which we attempted to match these data were variable, two aspects of our methodology allowed us to create a scale-independent relationship. We took a probabilistic approach to the likelihood of ALS data intercepting a branch or stem for discrete vertical slices, because ALS data are significantly sparser than TLS data, on the order of 10^1 ALS points per tamarisk patch versus 10^6 TLS points per patch. Stand structure values (i.e., vertical projected area) were summed and normalized by bed-parallel area of the patch. Hereafter, the term "patch" is used to describe the scale over which TLS data were collected and analyzed. Model development was based on observations made from the TLS patches (section 5.1.2).The term "window" is used to describe the scale over which the model was applied at the reach scale (section 5.1.3).

5.1.1. ALS Probability Maps

[36] Using a series of morphological filters, developed in part using the methodology of *Zhang et al.* [2003], the ALS data were classified as either bare ground or vegetation. Averaging 1.5 pts/m^2, we used the bare ground points to create a 0.5-m resolution, bare-earth digital elevation model (DEM) of the study areas. A 0.5-m DEM ensured sufficient topographic detail of the smallest patch (SC2, 6.5 m^2). The height above the bare ground of each vegetation point was determined as the difference between the elevation of each vegetation point and that of the ground surface. We took 0.20-m-thick horizontal slices of the ALS vegetation point cloud, corresponding to the 0.20-m horizontal slices used in the analysis of TLS data (section 4.1.2).

[37] Probability maps (0.5-m resolution) of the incidences of ALS points for each of the 0.20-m horizontal slices were created using indicator kriging [*Todd et al.*, 2003]. To construct probability maps, we used all LiDAR returns (i.e., ground and vegetation points) within the tamarisk-dominated floodplains and transformed them into indicator variables. For a given horizontal slice, those returns that were within the 0.20-m limits (e.g., between 2.0 and 2.2 m above the ground surface) were assigned a value of 1, while all other values for vegetation returns outside of the horizontal slice range and ground points were assigned a value of 0. As a result, each probability map provides a measure of the probability of a LiDAR pulse (ALS) being returned from vegetation at the associated height.

5.1.2. Creation of a Model to Link ALS to TLS

[38] We assumed that all the tamarisk-dominated stands in the two study reaches belonged to one of the three vertical projected area profile groups: sparse, moderate, or dense. For each of the three profile groups, we developed relations between height above the bed (H) and cumulative $A_{P,vert(n)}$ (Figure 8). Each of these relations was defined as a band with upper and lower bounds based on the cumulative $A_{P,vert(n)}$ curves of the 12 patches. Assignment of a patch into one of these three bands, and therefore as one of the three types of vertical projected area profiles (sparse, moderate, or dense), required knowledge of at least one height-dependent cumulative $A_{P,vert(n)}$ value. With the expressed goal of upscaling patch-scale observations using spatially robust ALS datasets, the height-dependent cumulative $A_{P,vert(n)}$ value must ultimately be derived from the vertical structure of the ALS data.

[39] ALS probability maps only provided us with an estimate of the likelihood that a branch or stem exists at a point

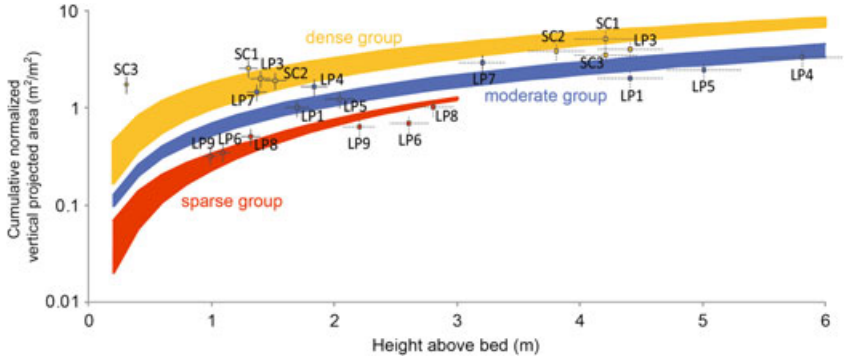

Figure 8. Space defined by height above the bed and normalized vertical projected area for the three projected area profile groups (sparse, moderate, and dense) and the predicted positions of the maximum and median $A_{P,vert(n)}$ of those TLS patches used to create the TLS-ALS model (Table 2). Bands were defined by the range in values measured from the 11 TLS patches. (LP2 was not included; see text for explanation.) This space was used to classify values extracted from the ALS data in the moving-window analysis. Horizontal error bars correlate to the 20% error in the predictive model, and vertical error bars correlate to the 6% error between stand height measured from ALS and TLS. Solid error bars are associated with predicted median values. Dashed error bars are associated with predicted maximum values. The SC and LP numbers refer to specific patches at Seacliff and Laddie Park, respectively.

on the floodplain. These maps did not provide us with a direct measure of the vertical projected area of tamarisk stands. To relate ALS probability maps to vertical projected area profiles derived from TLS scan data, we extracted the probability value from the ALS probability maps for every 0.20-m horizontal slice and applied those data to the centroid of each grid cell (section 4.1.2). Summed over the area of the whole patch, we quantified a vertical distribution of "blockage" (m^2/m^2), defined as a measure of vegetation density from the top-down perspective, for each patch,

$$Bk_{ALS} = \frac{\sum P(ALS)_{ij} \times A_{ij}}{A} \quad (14)$$

where $P(ALS)_{ij}$ is the probability extracted from the ALS probability map at the centroid of each polar grid cell, A_{ij} is the bed-parallel area of the cell, and A is the bed-parallel area of the TLS patch. From the vertical distribution of blockage, we constructed cumulative distribution curves of blockage from the ground to the maximum height of the vegetation in the patch. Both the cumulative Bk_{ALS} curves and cumulative $A_{P,vert(n)}$ curves were converted into cumulative frequency curves (Figure 9). We quantified $A_{P,vert(n)}$ and Bk_{ALS} quantiles from these cumulative frequency curves.

[40] For each patch, we calculated two H - $A_{P,vert(n)}$ values, the maximum and the median points (Table 2). The maximum value was the largest cumulative $A_{P,vert(n)}$ value ($A_{P,vert(n)(max)}$). This value necessarily occurs at the top of the vegetation canopy. The median value ($A_{P,vert(n)(50)}$) was identified as the 50th percentile of the cumulative $A_{P,vert(n)}$ distribution (Figure 9). The height at which the $A_{P(n)(50)}$ occurred was dependent on the profile shape and was not immediately apparent from the ALS data.

[41] To quantify these two points from ALS data, we determined the maximum height from the ALS data ($H_{ALS(max)}$) and calculated the maximum cumulative blockage ($Bk_{ALS(max)}$) (Figure 9). The relationship that we established between $Bk_{ALS(max)}$ and $A_{P,vert(n)(max)}$ was based on 11 of the 12 patches. We excluded patch LP2, where we determined that the canopy density was too thick to characterize the rest of the profile (Bk_{ALS}=1.8). We assumed that patches whose $Bk_{ALS(max)}$ values exceeded 1.5 m^2/m^2 belonged to the dense group. Based on the remaining 11 patches for $Bk_{ALS(max)} < 0.50$ m^2/m^2, a positive power law relationship exists between $Bk_{ALS(max)}$ and $A_{P,vert(n)(max)}$ (a=6.75, b = 1.92, R^2=0.76) while for $0.5 < Bk_{ALS(max)} < 1.5$ m^2/m^2, a negative relationship exists (a=2.24, b=−1.07, R^2=0.77). The presence of a threshold at 0.5 m^2/m^2 indicates that the canopy begins to filter out points greater than this value and that the lower portion of the plant is hidden from the ALS data acquisition process. Similar relationships were established between the maximum blockage ($Bk_{ALS(max)}$) and the median $A_{P,vert(n)}$ value ($A_{P,vert(n)(50)}$) for values of $Bk_{ALS(max)} < 0.50$ m^2/m^2 (a=13.5, b=1.92, R^2=0.76) and $Bk_{ALS(max)} > 1.5$ m^2/m^2 (a=2.98, b=−1.07, R^2=0.77) . These relationships allowed us to calculate both $A_{P,vert(n)(max)}$ and $A_{P,vert(n)(50)}$ from $Bk_{ALS(max)}$, a value derived from ALS data alone. Error between the quantified $A_{P,vert(n)(50)}$ ($A_{P,vert(n)(max)}$) and the predicted $A_{P,vert(n)(50)}$ ($A_{P,vert(n)(max)}$) using these relationships was approximately 20%. Additional relationships were established for $A_{P,vert(n)(25)}$ and $A_{P,vert(n)(75)}$ as a means of evaluating the shape of the $A_{P,vert(n)}$ profile, as explained below.

[42] To determine the height of $A_{P,vert(n)(50)}$, we identified a pattern in the relationship between the cumulative distribution of blockage and the cumulative distribution of $A_{P,vert(n)}$ for a given patch. These relationships reflect differences in the perspective from which the ALS and TLS data sets were collected; ALS data are collected from directly above (i.e., airborne) each area of vegetation, and TLS data are collected from a low-oblique perspective (i.e., a tripod). For patches whose maximum tree heights were greater than or equal to 5 m, $Bk_{ALS(50)}$ occurred 2.3 m (sd=0.02) higher in the profile than $A_{P,vert(n)(50)}$. For patches whose maximum heights were between 4 and 5 m, the difference was 1.4 m (sd=0.2). For patches whose maximum height was less than 4 m, the difference was 0.2 m (sd=0.2) (Table 2).

[43] Accounting for the 20% uncertainty in quantified and predicted $A_{P(n)}$ values (horizontal error bars), and a 6% difference in the maximum height of the vegetation (Table 2) within a patch between TLS and ALS (vertical error bars), we predicted the correct $A_{P,vert(n)}$ profile group (i.e., sparse, moderate, or dense) for 9 of the 11 patches using the H_{50} - $A_{P,vert(n)(50)}$ values and 6 of the 11 patches using the H_{max} - $A_{P,vert(n)(max)}$ values (Figure 8). On average,

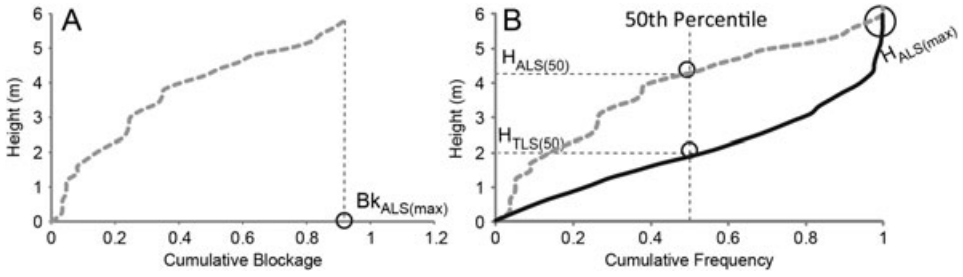

Figure 9. Cumulative curves used to relate TLS data to ALS data. Example is shown for patch LP4. (A) Cumulative maximum blockage ($Bk_{ALS(max)}$) occurs at the maximum height from the ALS data ($H_{ALS(max)}$). (B) Cumulative frequency curve for $A_{P,vert(n)}$ (solid black line) and $Bk_{(ALS)}$ (dashed gray line). The median values of $A_{P(n)}$ and $Bk_{(ALS)}$ were used to define the median heights for the $H_{TLS(50)}$ and $H_{ALS(50)}$ from the cumulative frequency curves, respectively. A relationship between the heights at which the median values occurred at a single patch for the $A_{P(n)}$ and $Bk_{(ALS)}$ was identified that was subsequently used in the application of the TLS-ALS model to the reach scale.

Table 2. Measured and Predicted Tamarisk Height (H), ALS Blockage ($Bk_{(ALS)}$), and Normalized Vertical Projected Area ($A_{P,vert(n)}$) Values for 12 Vegetation Patches Used in the Development of the ALS-TLS Model

	Measured							Predicted		
	Maximum				Median			Maximum	Median	
	$H_{TLS(max)}$	$A_{P,vert(max)}$	$H_{ALS(max)}$	$Bk_{ALS(max)}$	$H_{TLS(50)}$	$A_{P,vert(50)}$	$H_{ALS(50)}$	$A_{P,vert(max)}$	H_{50}	$A_{P,vert(50)}$
Patch	(m)	(m^2/m^2)	(m)	(m^2/m^2)	(m)	(m^2/m^2)	(m)	(m^2/m^2)	(m)	(m^2/m^2)
LP1	4.4	1.88	4.4	1.37	1.5	0.94	3.10	1.60	1.70	1.00
LP2	5.9	5.13	5.7	1.79	2.0	2.57	4.25	-	-	-
LP3	4.4	4.20	4.8	0.75	1.5	2.10	2.80	3.05	1.40	2.00
LP4	5.8	2.54	5.8	0.89	1.8	1.27	4.14	2.55	1.84	1.65
LP5	5.0	3.06	5.2	1.15	2.3	1.53	4.35	1.93	2.05	1.23
LP6	2.6	0.67	2.6	0.21	1.2	0.34	1.25	0.35	1.09	0.35
LP7	3.2	1.94	3.4	0.45	1.4	0.97	1.53	1.46	1.37	1.45
LP8	2.8	0.75	2.8	0.26	1.2	0.38	1.48	0.51	1.32	0.51
LP9	2.2	0.74	2.2	0.20	1.1	0.37	1.15	0.32	0.99	0.32
SC1	4.2	5.40	3.0	0.61	1.4	2.70	2.70	3.84	1.30	2.55
SC2	3.8	3.11	3.2	1.11	1.2	1.56	1.75	3.82	1.52	1.91
SC3	4.2	4.17	3.8	0.40	1.9	2.09	1.70	3.48	0.30	1.74

[a]$Bk_{ALS(75)}/Bk_{ALS(25)}>7$ indicates high canopy blockage, predicted value increased by 50%.

the $A_{P,vert(n)(50)}$ was overpredicted by 0.22 m^2/m^2, while the $A_{P,vert(n)(max)}$ was underpredicted by 0.28 m^2/m^2.

[44] The discrepancy between data collected from a top-down perspective and that collected parallel to the flow is greatest for dense canopies. $A_{P,vert(n)}$ values for SC2 and SC3 were significantly underpredicted by the model. We attribute this divergence in model success to an extremely dense canopy, where the ratio between $Bk_{ALS(75)}$ and $Bk_{ALS(25)}$ is relatively large. For SC2 and SC3, this ratio was greater than 7, while for the remaining nine patches, the ratio was on average 2. In patches such as SC2 and SC3, the density of the top of the canopy essentially shadows the lower portion of the profile, thereby altering the cumulative blockage curve. We determined that an adjustment of 50% from the predicted value was appropriate to correct for the canopy blockage.

5.1.3. Application of the Model

[45] With these relationships established, we extended the patch-scale observations to the entire study area. To do this, we used a 2-m, 3-m, and 4-m circular moving window. Within each moving window, we summed the blockage values derived from the ALS probability maps. The window was used as a proxy for the patch. We used various window sizes to determine the best scale over which to apply the ALS-TLS model. Both the maximum and median H_{ALS} - $A_{P,vert(n)}$ values were calculated in order to provide the best gage for the patch type to which each discrete window belonged. The 50% correction was applied to those profiles that had a predicted ratio of $Bk_{ALS(75)}/Bk_{ALS(25)}$ greater than 7.

[46] A 2-m grid overlaying the study area extracted the summed probabilities at the center of each grid cell. We applied the same methodology as described in section 5.1.2 to extract maximum height, maximum blockage, and the height and value of the quartile values of blockage over the window. We classified the two reaches by the type of vertical projected area profile and therefore the type of depth-dependent roughness profile, based on these values and the empirical models that link $Bk_{ALS(max)}$ to $A_{P,vert(n)(max)}$ and $A_{P,vert(n)(50)}$.We estimated the various metrics for modern alluvial deposits that were dominated by tamarisk and did not apply the model to areas of vegetation dominated by other species, such as box elder.

[47] Thus, we applied our TLS relations to the two study reaches, based on the ALS data, the result of which was a map of vegetation density (i.e., classified into the three profile groups: sparse, moderate, or dense) present within each map cell (Figure 10). We evaluated the model, and the size of the moving window, by comparing the model predictions of conditions in the 12 patches to those estimated from the ALS data (Figure 10 and Table 3). Because individual patches are larger than the scale of the grid (4 m^2), the roughness map consisted of multiple grid cells within each patch. We acknowledge that the discrepancy in scale, both between patch and window sizes as well as between patches and the grid over which we validated the model, inevitably resulted in differences in model prediction. For example, if a 50-m^2 patch is evaluated using a 2-m circular window (12.5 m^2), the stand structure of sections of this patch, while characterized as one group in the development of the model, may belong to two or more groups. Variability in density existed within a given patch. While averaging during model development masked density differences, this patch-scale variability was highlighted during model application, especially when using different window sizes.

5.2. Upscaling Results and Interpretation

[48] The moderate and dense patches were best captured with a moving window of 3 m (Table 3). The model correctly classified 84% and 70% of the cells within the three moderate and five dense patches, respectively. In contrast, the sparse patches performed the best when the moving window was 4 m; the success rate in this case was 42%. However, the difference in performance for the sparse patches did not vary greatly for the different window sizes (36% and 35% for a 2-m and 3-m moving window, respectively). The sparse patches had the lowest success in application of the ALS-TLS model. Based on the above findings, we considered that the 3-m window was best applied to these study reaches.

[49] Classified maps of the Laddie Park and Seacliff reaches qualitatively showed good agreement with field

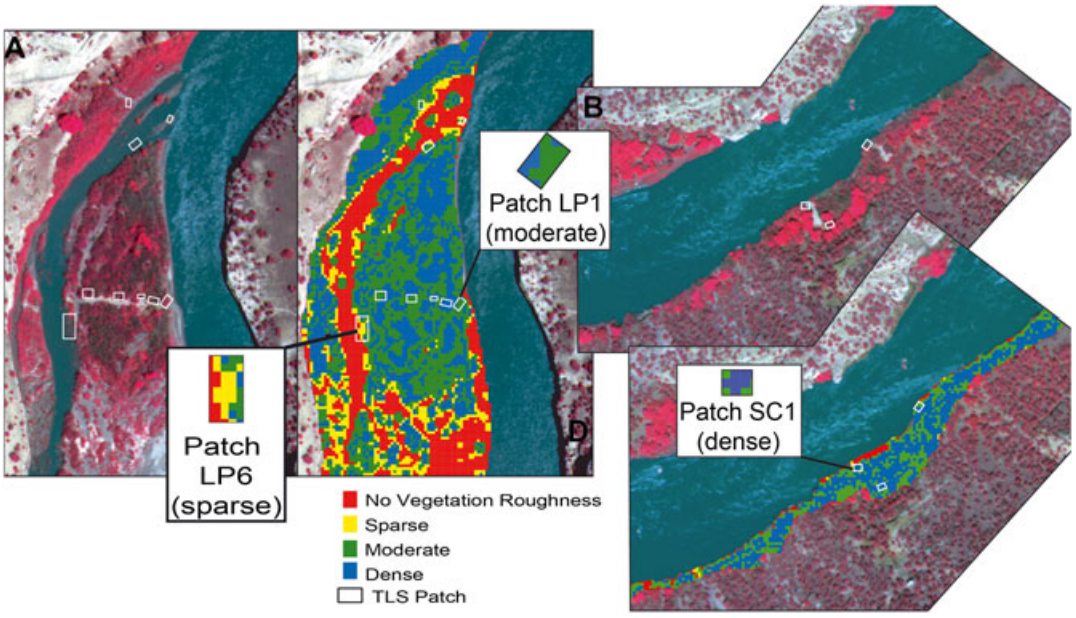

Figure 10. Application of the TLS-ALS model (with a 3-m moving window) to the (A) Laddie Park and (B) Seacliff reaches. The pattern of profile group recognition is generally realistic. We evaluated the model based on the correct prediction of group type for each 2-m square cell within the 12 vegetation patches.

Table 3. Percentage of 2-m Cells Within the 12 TLS Patches That Match the TLS Profile Group in the Application of the TLS-ALS Model Using a 2-m, 3-m, and 4-m Moving Window

Profile Group	2-m Moving Window	3-m Moving Window	4-m Moving Window
1. Sparse	36%	35%[a]	42%
2. Moderate	46%	84%	58%
3. Dense	52%	70%	60%

[a]Within-patch spatial variability of $A_{P,vert(n)}$ profiles, analyzed at the same 3-m moving window scale as the TLS-ALS model application, increases model prediction to 65%.

observations (Figure 10). Generally, the sparse group was restricted to low-elevation gravel bars. These stands only occur in the Laddie Park reach. The tamarisk stands in the Seacliff reach were predominantly established on eddy bars and are denser. Many individuals in these groups are buried by more than 1 m of fine sediment. Moderate and dense stands also occur in the Laddie Park reach on higher topographic surfaces. Thick deposits in the central parts of the islands support relatively dense tamarisk stands.

[50] The discrepancy in scale, both between TLS patch and moving window ALS model sizes and between patches and the grid over which we validated the model, inevitably contributed to differences in model prediction of stand type within the 12 TLS patches, especially for the sparse patches. Spatial variability exists within a TLS patch, and, therefore, the larger the size of the patch, the greater the expected variability in predicted $A_{P,vert(n)}$ groups within that patch. We expect there to be the greatest within-patch variability in the sparse-group patches. Extraction of $A_{P,vert(n)}$ profiles from the TLS scan data over the same scale of TLS-ALS model application (i.e., the 3-m window) increased the match in $A_{P,vert(n)}$ group type for the sparse groups from 35% to 65% (Table 3). Additionally, cells located closest to the scanner had greater success, highlighting the difficulty in capturing large areas with TLS.

[51] Future work might be able to fine-tune these upscaling relationships and/or more robustly validate their application at particular sites and/or their transferability to other fluvial settings. While the methodology could be developed using a smaller TLS patch size, and potentially a greater number of patches, one must be cognizant of the impact of patch size on identification of the within-patch processes (e.g., routing of flow around individual stems that influence the larger, reach-scale flow field) (discussed further in section 6.1). Additionally, greater spatial congruity between patch and moving window size would likely result in increased predictive success. However, an increase in the size of the window to more closely match patch size would result in unreasonable averaging across vegetated/unvegetated areas and the locations of high variability in vegetation density.

6. Discussion

6.1. Verification and Uncertainty of Patch-Scale Values

[52] To verify the vertical projected areas we determined from our TLS measurements, we compared our values with direct field measurement of tamarisk and willow in other studies. The majority of studies that report vegetation densities do so at the reach scale as stem densities (e.g., number of stems/ha) [e.g., *Stromberg et al*., 1993; *Beauchamp and Stromberg*, 2007]. These bulk values mask the fine spatial resolution that we captured in our study. However, a few studies report values collected over spatial scales comparable to the patch scale. *Griffin et al*. [2005] found that tamarisk stems greater than 0.01 m in diameter on the Rio Puerco in New Mexico were spaced 0.20 m apart, and, therefore, have an $A_{P,vert(n)}$ value of 0.25 m^2/m^2 at a height of 1 m. Detailed stem measurements of young sandbar willow (<10 years) growing on a gravel bar on the upper Colorado

River had $A_{P,vert(n)}$ values that ranged between 0.06 and 0.14 m^2/m^2 at a height of 1 m [*Logan*, 2000]. Values for sandbar willow on tributaries of the South Platte River, Colorado, ranged between 0.08 and 0.93 m^2/m^2 at a height of 1 m [*Griffin and Smith*, 2004]. Generally, the range of values from these studies fits within the range of $A_{P,vert(n)}$ values quantified for the 12 patches of this study (0.06–0.37 m^2/m^2 at a height of 1 m).

[53] Without independent, non-TLS field measurements of stand structure, we cannot assign a degree of uncertainty or estimate of error to the vegetation densities calculated in this paper. Nevertheless, prior studies provide information on the potential accuracy of the approach used in our investigation. In the development of the methodology employed here, *Straatsma et al*. [2008] measured stem densities for 23 plots. They determined that their modeling efficiency was 63%. Errors were attributed to (1) the assumption of randomly distributed stems in the development of the methodology, (2) the presence of leaves at the single elevation measured, and (3) the relatively low resolution of their scans. However, differences exist between our study and that of *Straatsma et al*. [2008], which preclude direct extension of their reported uncertainties to our work. For one, the types of vegetation analyzed in the two studies differ greatly, from a sparse stand of straight-stemmed willow (*Salix alba*) [*Straatsma et al*., 2008] to a densely vegetated stand of tamarisk with randomly oriented stems (this study). As such, the assumption of randomly distributed stems might introduce less error to our study, especially for the moderate to dense stands. We acknowledge that measurement of structure of tamarisk stands during the growing season adds some error to the measurements due to the presence of leaves. However, the stem area to leaf area ratio for tamarisk is relatively high and unlikely to exert a major influence. Finally, the resolution at which *Straatsma et al*. [2008] scanned was much coarser than ours: 238–1104 pulses per angular degree [*Warmink*, 2007] versus 1005–3016 pulses per angular degree. This increased density of points has a greater likelihood of capturing all stems. Additionally, we limited our scanned patches to relatively small footprints, thereby limiting shadowing of stems. It should be emphasized that our goal with this research was not to build a highly precise model of vegetation density, but rather to find a reasonable proxy for vegetation density that can be used to estimate its effect on floodplain hydraulics.

[54] We back-calculated the drag coefficient (C_D) from the drag force equation as a way to relate stand structure (vertical projected area profiles) to roughness. For vertical cylinders, a C_D value between 1.0 and 1.2 is regularly cited as the most reasonable value for the range of flow conditions used in experimental work [e.g., *Jarvela*, 2004]. A large literature exists that explores ways in which these values may be predicted or adjusted given the range of variability of natural conditions. *Nepf* [1999] found that for an increase in density of cylindrical "stems," the bulk C_D decreased from 1.2 to less than 0.4. In a series of flume experiments using willow, *Jarvela* [2002] calculated C_D values that averaged between 1.6 and 1.4 depending on the spacing and distribution of the willow. Other studies using real stems [*James et al*., 2004] or measuring drag in a noncontrolled, field-based setting [*Hygelund and Manga*, 2003; *Manners et al*., 2007] have reported a much larger range and maximum values, as high as 20. Average C_D values in our study (1.0 for all groups with flow depth < 1.0 m and 1.3, 1.1, and 1.5 for the sparse, moderate, and dense groups, respectively for flow depths ≥ 1.0 m) fall well within this range of experimentally determined drag coefficients.

6.2. Hydraulic Roughness of Tamarisk

[55] The increase in hydraulic roughness associated with colonization of bare alluvial deposits by tamarisk has been suggested as an important cause of channel narrowing of the Colorado River and its tributaries [*Graf*, 1978; *Birkeland*, 2002]. However, few studies have quantified the change in hydraulic roughness.

[56] In this study, we estimated the large-scale distribution of roughness of tamarisk patches. Patch-scale Manning's *n* values ranged from 0.057 to 0.319. The higher end of these values is greater than those generally reported for vegetated floodplains (upwards of 0.25) that are often calculated from the hydraulic conditions (water surface slope and depth) for small reaches or whole floodplain surfaces [*Barnes*, 1967; *Arcement and Schneider*, 1989; *Sandercock and Hooke*, 2010]. Averaging conditions over these areas inevitably accounts for spatial variability in roughness values. In contrast, we calculated roughness values over smaller spatial scales. Our values are therefore representative of the local resistance of vegetation and are solely applicable to the patch scale.

[57] When we compare our predicted patch-scale Manning's *n* values to those determined experimentally for tamarisk stands, we find good agreement. The sparse group best represents the types of plants used in experimental studies. Our predicted values (0.076–0.141) fall within the range of experimentally determined values (0.055–0.180) [*Freeman et al*., 2000; *Fathi-Maghadam et al*., 2011]. Specifically, we identified the experimental conditions in *Freeman et al*. [2000] that most closely match our two-dimensional models and found excellent agreement (Figure 7).

[58] We found that roughness increases with flow depth, generally scaling with the vertical projected area of vegetation patches. This finding is consistent with experimental work [*Fathi-Maghadam and Kouwen*, 1997; *Musleh and Cruise*, 2006]. *Musleh and Cruise* [2006] reported that roughness through a patch of partly submerged rigid cylindrical rods increases linearly with flow depth from 0.06 to 0.24. However, while other studies documented a linear increase in roughness with depth, we found that roughness increases in proportion to changes in the vertical projected area. As expected, roughness decreases as patches become submerged (Figure 7). For sparse density stands, total patch roughness decreased after a stand was completely submerged.

[59] Often, hydraulic models assume that roughness decreases as flow depth increases [*Arcement and Schneider*, 1989]. This assumption is applicable for in-channel conditions either where no vegetation exists or where vegetation becomes fully submerged. The declining contribution of bed roughness to total patch roughness with increasing flow depths supports the applicability of the above assumption (Figure 7). However, for floodplain flows through stands of tamarisk and willow, and likely other types of shrubby riparian vegetation, our results predict that total patch roughness increases with increasing flow depth because cumulative vertical projected area also increases with increasing flow depth.

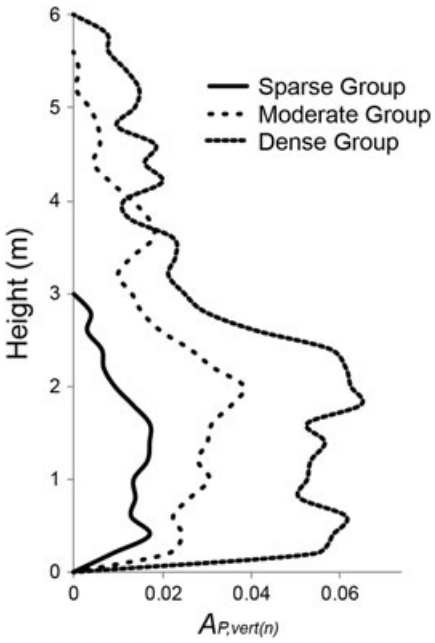

Figure 11. Group-averaged normalized vertical projected area profiles.

[60] Group-average normalized vertical projected area profiles (Figure 11) indicate that the profile shapes for moderate and dense patches are similar, although the magnitude of projected area is greatest for dense patches. Both have maximum values around 2 m above the ground surface. However, the profiles differ within 0.5 m of the ground surface. Here, there is a second maximum $A_{P,vert(n)}$ value in densely vegetated patches, on average three times greater than that of the moderate patch. We hypothesize that this difference may be attributed to patch-scale organization (Figure 12).

[61] Densely vegetated patches may promote more well-defined flow pathways and channels that occur between clumps of dense vegetation. A feedback between dense clumps of stems close to the ground surface and strong flow paths likely exists [*Corenblit et al*., 2007]. Dense clumps redirect and channelize flow, scouring out new vegetation and maintaining flow paths. Higher velocities in these flow paths have the potential to shear low-lying stems. When tamarisk stems break, a greater number of stems regrow, thereby creating greater stem density. Additionally, because these flow paths are more well defined and have a larger proportion of the flow, and therefore faster velocities, they are capable of transporting woody debris, some of which may become trapped by stems. Field observations of woody debris in and around dense group patches support this notion. All of these factors contribute to high stem density close to the ground (Figure 12).

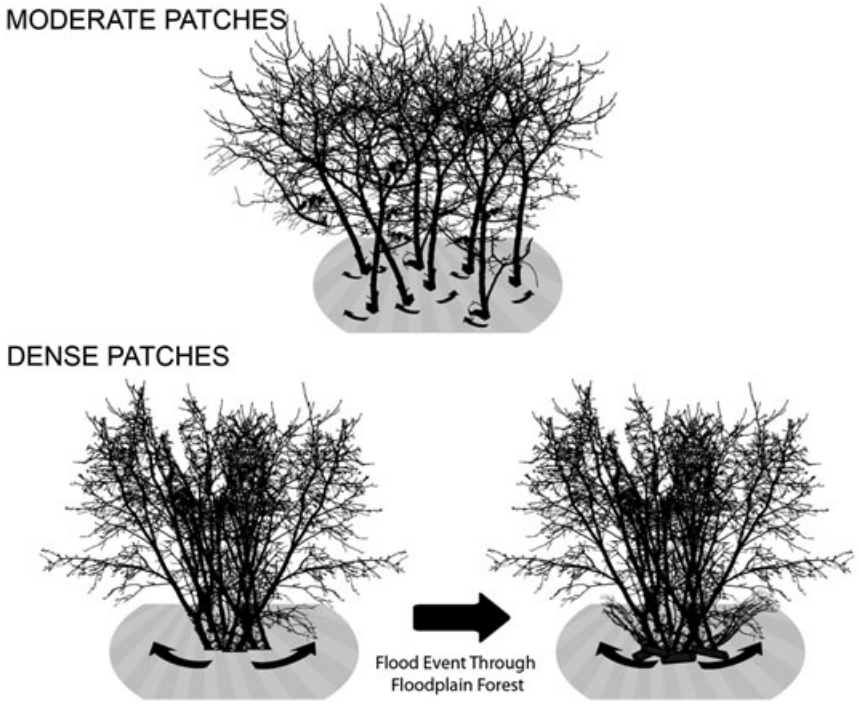

Figure 12. Cartoon showing the interaction between tamarisk patch density and flow. Stem spacing influences the size and strength of flow paths around and through the patch. If stems are clumped together, the flow will be channelized, shearing low-lying stems and delivering wood. A greater number of stems will grow back after being sheared, all of which results in higher stem density and therefore greater vertical projected area in the 0.5 m above the ground surface. The density and spacing of stems also has an influence on the hydraulics of flow through a patch (i.e., on the C_D). These relationships suggest that feedbacks exist among flow and tamarisk growth. It is these feedbacks that control the spatial pattern of vegetation hydraulic roughness.

[62] Similarly, the sparse group profile shows the same characteristic secondary peak close to the ground. These patches grow on gravel bars along the edge of, or even within, high-flow side channels. High velocities often shear stems here and deliver woody debris. Thus, similar processes may be attributed to determining the shape of the profile. However, the magnitude of these processes and location within the channel prevents the sparse group from growing to the same density.

[63] The fact that the moderate density patches are generally composed of evenly spaced stems, while dense (and sparse) patches tend to have clumps of stems between larger open areas has a direct impact on the hydraulic effectiveness of these two patch types. An extensive literature exists on the hydraulic impact of stem spacing [e.g., *Nepf*, 1999; *Stone and Shen*, 2002; *Liu et al*., 2008]. Generally, closer spacing among stems reduces the bulk drag coefficient due to the downstream "sheltering" effect [*Raupach*, 1992]. We might attribute the lower average C_D value for moderate patches (1.1 as compared to 1.5 for dense patches and 1.3 for sparse patches) to this effect, whereby the arrangement of stems in a moderate patch (Figure 12) increases the wake interference.

[64] We do not know if tamarisk patches get denser or sparser as they age, but we have observed changes to tamarisk patches as a result of the aggradation of fine sediment. Tamarisks on gravel bars remain short and sparse as the stands age, presumably because of the harsh hydraulic environment. However, we have observed that tamarisk stands that established on gravel bars, but are now buried by as much as 3 m of fine sediment, have moderate or dense vertical projected area profiles. Fine sediment deposition on gravel bars may be a result of an increase in the local hydraulic roughness, an indication of an alteration to the flow field, or of a change in the hydrology and/or sediment load that has resulted in sediment surplus. In the study reaches, we find fine-grained caps on gravel bars in areas whose hydraulic setting (e.g., upstream from tight bedrock bends) promotes deposition. However, these caps were not as spatially extensive prior to the establishment of tamarisk and willow. The caps have been increasing in size with the expansion of riparian vegetation. This observation suggests that within certain hydro-geomorphic environments, establishment of vegetation increases hydraulic resistance and promotes deposition of fine sediment. Fine-grained alluvial deposits provide additional surfaces for the colonization of new plants. Additionally, field observations from floodplain trenches indicate that fine sediment deposition increases the density of tamarisk stands. Greater coverage and density of tamarisk further increase vegetative hydraulic resistance, altering flow fields, and promoting deposition of fine sediment. Thus, feedbacks exist among flow, sediment, and tamarisk growth. It is these feedbacks that control the spatial pattern of vegetation hydraulic roughness.

6.3. Upscaling the Hydraulic Roughness of Patch-Scale Observations

[65] As an illustration of how a reach-scale evaluation of the impact of vegetation on the flow field might be pursued, we applied the methodology described in this paper to a two-dimensional hydraulic model evaluated over the entire Laddie Park site. Our goal was to illustrate the importance of incorporating a spatially variable representation of vegetation roughness. We applied the stage-dependent roughness curves established for the study sites (Figure 7) to the two-dimensional hydraulic model River2D.

[66] A combination of LiDAR-derived topography, acquired in 2008, and real time kinematic global positioning system (RTK GPS)-based bathymetric surveys, acquired in 2010, were used to create a DEM that was sampled onto a triangular finite element mesh with 2-m node spacing around the tamarisk-dominated floodplains and 10-m node spacing elsewhere. A constant discharge upstream boundary condition was established for two flood discharges, 450 and 935 m^3/s, and a constant downstream water surface elevation was specified. Because a rating relation was not available to use for specifying flow boundary conditions, downstream water surface elevations were derived from a one-dimensional Hydraulic Engineering Centers River Analysis System (HEC-RAS) [*U.S. Army Corps of Engineers*, 2008] model run under steady, subcritical flow conditions with a normal depth boundary condition (water surface slope of 0.001). For context, base flows are approximately 15 m^3/s; a 450 m^3/s flood has a recurrence of approximately 5 years, and a 935 m^3/s flood is the flood of record whose recurrence is greater than 100 years [*Elliott and Anders*, 2004].

[67] Roughness in the model is provided in terms of a roughness height (k_s). While the roughness height of the bed does not change with flow depth [*Whiting and Dietrich*, 1990], we determined in section 4 that the roughness, as measured by Manning's n, of a patch of tamarisk changes with flow depth. To account for the changing roughness over the flow depth, we converted group-specific roughness profiles into k_s values based on equation (3).

[68] We ran two scenarios for each of the two discharges:

1. Constant roughness for the entire reach ($k_s = 0.1$ m)
2. Assignment of stage-dependent, spatially variable roughness as determined for vegetated areas using the ALS-TLS model. We used the relationships established between $Bk_{ALS(max)}$ to $A_{P,vert(n)(max)}$ and $A_{P,vert(n)(50)}$ and the stand height to determine the vegetation density (Figures 8 and 9). The classified map is shown in Figure 10. With a known vegetation density group, we assigned the corresponding roughness profile (Figure 7). Unvegetated areas were assigned values of $k_s = 0.4$ m for gravel and $k_s = 0.1$ m for pools/bare sandbars. Unvegetated areas were delineated based on aerial photographs and ground surveys.

[69] Model validation was based on a few field measurements made at 450 m^3/s in spring 2011. We took discharge measurements with a Teledyne RD Instruments RiverRay (acoustic Doppler current profiler (ADCP) in the side channel (river left) of the study site at 450 m^3/s. These measurements are in good agreement with model output (4% difference from the total discharge of scenario 2).

[70] The extent of floodplain inundation was slightly sensitive to the addition of spatially variable depth-dependent roughness at 450 m^3/s (Figure 13). The average water depth through the reach differed by less than 0.30 m for both discharges. However, the various model runs using different scenarios show that prediction of the distribution of bed shear stress differs in important ways (Figure 13). Characterization of the spatial distribution of shear stress is a critical component

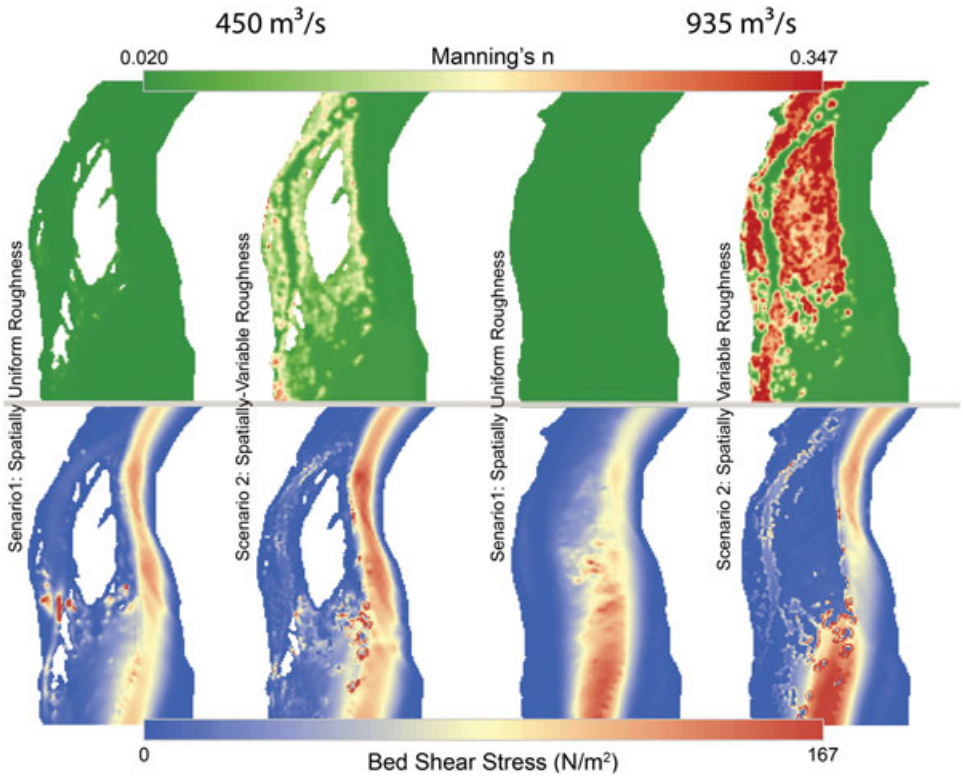

Figure 13. Two-dimensional model output at the Laddie Park reach for two discharges (Q=450 and 953 m^3/s) and two roughness scenarios. (1) Spatially uniform roughness: A constant k_s value was assigned to the reach. When converted to n, these values varied slightly as a result of the depth dependence of this relationship. (2) Spatially variable roughness: Application of the TLS-ALS model expressly accounts for stand structure in the parameterization of roughness. A constant k_s value was assigned separately to pools/sandbars and to gravel bars/riffles. When converted to n, these values varied slightly as a result of the depth dependence of this relationship. (Top) The resulting maps of roughness (shown here as Manning's n) for the two scenarios at the two discharges. (Bottom) The near-bed shear stress (τ_b).

in the prediction of the divergence of the sediment transport field and in the prediction of the distribution of scour and fill that causes channel narrowing or widening. The shear stress predicted by River2D is the total boundary shear stress, τ_o, and is the sum of the stress exerted on the vegetation, τ_{veg}, (i.e., form drag) and the stress exerted on the bed and banks, τ_b, (i.e., skin friction) [*Buffington and Montgomery*, 1999; *Smith*, 2004]. We are interested in extracting the latter component, τ_b, because of its geomorphic importance in sediment transport.

[71] The proportion of τ_o from τ_{veg} and τ_b may be assigned based on the forces exerted on the stems and on the bed, respectively, in the two-dimensional patch model. In the process of quantifying the vegetative and whole patch roughness in section 4.2, we quantified the force exerted on the bed, F_{bed}, and the force exerted on the stems, $F_{D,veg}$. We determined $F_{D,veg}/F_{bed}$ as a function of flow depth for each of the three vertical projected area profile groups (i.e., sparse, moderate, and dense) (Figure 14). As stress is the force per unit area, the force ratios for each vegetation group also specify corresponding τ_{veg}/τ_b ratios. We draped the density classification for vegetation patches, as determined by the TLS-ALS model (Figure 10), over River2D τ_o output and applied the τ_{veg}/τ_b ratio, unique to each group, to quantify the near-bed shear stress (Figure 13).

[72] The general patterns of vegetative roughness and the resulting near-bed shear stress values predicted through the application of the methodology developed in this paper appear reasonable based on field observations, aerial photograph analyses, and an intimate knowledge of the site [*Manners et al*., 2011]. Incorporation of a spatially variable representation of vegetation roughness exposes regions of very low near-bed shear stresses (Figure 13) that correlate with thick deposits of fine-grained alluvium. Differences in the pattern of near-bed shear stress between the spatially uniform and spatially variable roughness are more pronounced for the higher discharge (935 m^3/s), because the water accesses the vegetated floodplain. This example of the Laddie Park site is a proof of concept that we can use the fusion of TLS and ALS data across multiple scales. Such a multiscalar analysis provides a platform to more robustly explore the mechanisms and feedbacks between vegetative encroachment into active alluvial surfaces and the geomorphic responses.

7. Summary and Conclusions

[73] The methodology described here demonstrates the feasibility of incorporating small-scale interactions between water and stems into a larger scale process-based evaluation of the role of riparian vegetation on the flow field. To our knowledge, the multiscalar analysis presented here is the first to mechanistically account for shrubby riparian vegetation stand structure, and associated hydraulic roughness of

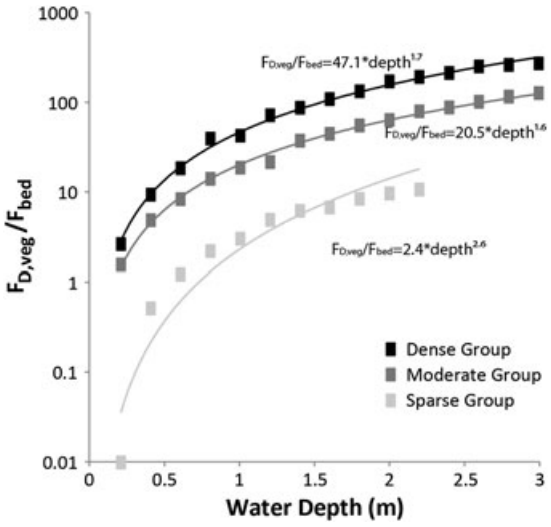

Figure 14. Depth-dependent ratio of forces on the stems to those on the bed ($F_{D,veg}/F_{bed}$) for each of the three vertical projected area profile groups (i.e., sparse, moderate, and dense). As stress is the force per unit area, we used the $F_{D,veg}/F_{bed}$ ratios to partition total boundary shear stress into the stress exerted on the vegetation, τ_{veg}, (i.e., form drag) and the stress exerted on the bed and banks, τ_b, (i.e., skin friction). The fitted curves had R^2 values of 0.91, 0.99, and 0.99 for the sparse, moderate, and dense groups, respectively.

vegetation patches, at the reach scale. Vegetation metrics that have been repeatedly shown to affect the flow field, including stem density and spacing [e.g., *Nepf*, 1999; *Bennett et al*., 2002; *Jarvela*, 2002], were implicitly incorporated in a spatially explicit way into the larger scale parameterization of vegetation. Although we applied this parameterization to a reach, the ALS data we used could have been applied to the entire Yampa and Green River corridors within Dinosaur National Monument. Through incorporation of this finer scale detail derived from the TLS data, we believe that the methodology presented here has the potential to capture the impact of riparian vegetation on the flow field in a detailed and spatially explicit way at a large scale.

[74] Our study formulated a methodology that takes advantage of the increasing availability of spatially extensive data sets, such as ALS, as well as the accessibility of high-resolution point clouds from TLS. We present one possible way to relate the stand structure of discrete patches of vegetation derived from high-resolution measurements to the much coarser signature of stand structure derived from airborne data. Thus, the goal of this methodological development has been to capture the detailed structure of riparian vegetation and extrapolate those influences out over large areas. Adoption of the specific relationships formulated here may not necessarily be possible for other vegetation communities; however, the methodology presented here probably transcends geographic location and vegetation community composition.

[75] Results from this work predict that the roughness of forested floodplains increases with flow depth. With rising stage, the hydraulic resistance of the floodplain increases until the vegetation is fully submerged; thereafter, roughness declines. This prediction supports experimental observations and implies that reach-scale dynamics over a flood event are continually being altered by the interaction of water and vegetation.

[76] Although there are a variety of other approaches that can be used for modeling the hydraulic impact of vegetation [e.g., *Nepf*, 1999; *Kean and Smith*, 2004], a key contribution of this study is the description of a multiscalar model. Application of our TLS-ALS model to a two-dimensional hydraulic model of Laddie Park highlights the fact that assigning spatially explicit, stage-dependent hydraulic roughness values has the potential to reveal geomorphically relevant hydraulic patterns at the reach scale that would not be apparent with simpler characterizations of channel or vegetation roughness. Ultimately, detection of geomorphically relevant patterns at these scales provides a first step in the identification and prediction of vegetation for both inducing and exacerbating channel change.

[77] The role of riparian vegetation in causing channel change is an enduring and pervasive question in river management. For example, the Colorado River basin has been plagued by the invasion of tamarisk. The rapid establishment and dominance of this species has contributed to profound channel narrowing and cross-section simplification to the detriment of in-channel habitat critical to the survival of some native fish species [*Olden et al*., 2006]. The two-dimensional hydraulic floodplain models developed with spatially variable, stage-dependent roughness described here have the potential to reveal areas sensitive to further channel change and ultimately to build predictive morphodynamic models of channel evolution.

Notation

A	bed-parallel area, m^2
A_{ij}	bed-parallel area of a cell, m^2
$A_{P,vert}$	flow-perpendicular projected area, m^2
$A_{P,vert,ij}$	flow-perpendicular projected area of a cell, m^2
$A_{P,vert(n)}$	maximum, cumulative, flow-perpendicular, normalized projected area, [−]
α	depth of the cell along the radial distance from the scanner, m
B_{ij}	number of points intercepted between the scanner and the cell, [−]
Bk_{ALS}	ALS blockage, [−]
C_D	drag coefficient, [−]
$\delta(x)$	stem deflection in the streamwise direction, m
d	stem diameter, m
D_v	vegetation density, m^{-1}
$D_{v,ij}$	vegetation density of a cell, m^{-1}
E	stiffness modulus, N/m^2
F	external or internal forces, N
$F_{D,veg}$	vegetative drag force, N
G_{ij}	number of points intercepted within a cell, [−]
g	gravitational acceleration, m/s^2
H	tamarisk height above the bed, m
H_{ALS}	tamarisk height measured from ALS data, m
H_{TLS}	tamarisk height measured from TLS data, m
I	cross-area inertial modulus, m^4
k_s	effective roughness height, m
n	Manning's roughness value, [−]

n_{bed}	Manning's bed roughness value, [−]
n_{patch}	Manning's patch roughness value, [−]
$n_{vegetation}$	Manning's vegetation roughness value, [−]
p	hydrostatic pressure, Pa
ρ	density of water, kg/m^3
φ	angular distance, degrees
T_{ij}	total number of emitted laser pulses that passed through the distal boundary
τ_0	total boundary shear stress, N/m^2
τ_b	shear stress on bed, N/m^2
τ_{veg}	shear stress on vegetation, N/m^2
U	depth-averaged velocity, m/s
U_r	depth-averaged reference velocity, m/s
y	flow depth, m
z	vertical height of the cell, m

[78] **Acknowledgments.** Many individuals helped with field logistics and data collection efforts. We have benefited from the continual support and encouragement of Tamara Naumann and others on the staff of Dinosaur National Monument. The TLS data acquisition was funded by a U.S. Geological Survey Grant to develop a Big River Monitoring Protocol for the National Park Service's Northern Colorado Plateau Network. This research was funded by a Quinney Fellowship and National Science Foundation Doctoral Dissertation Improvement Grant to the lead author. Additional support was provided by Utah State University and the United States Geological Survey—Grand Canyon Monitoring and Research Center. We owe thanks to James Brasington and Rebecca Hodge, whose original work on TLS patch scanning [*Hodge et al*., 2009], and upscaling patch-scale discrete element model results to drive reach-scale reduced complexity models [*Hodge et al*., 2007], served as a conceptual seed for the upscaling approaches we pursued here. The manuscript's clarity and organization was greatly improved thanks to the helpful and constructive reviews of Steve Darby, John Buffington, and two anonymous reviewers.

References

Allred, T. M., and J. C. Schmidt (1999), Channel narrowing by vertical accretion along the Green River near Green River, Utah, *Geol. Soc. Am. Bull.*, *111*(12), 1757–1772.

Antonarakis, A. S., K. S. Richards, J. Brasington, M. Bithell, and E. Muller (2008), Retrieval of vegetative fluid resistance terms for rigid stems using airborne lidar, *J. Geophys. Res.*, *113*, G02S07, doi:10.1029/2007JG000543.

Arcement, G. J., and V. R. Schneider (1989), *Guide for Selecting Manning's Roughness Coefficients for Natural Channels and Flood Plains*, Federal Highway Administration, U.S. Department of Transportation, Washington, D. C.

Auble, G. T., J. M. Friedman, and M. L. Scott (1994), Relating riparian vegetation to present and future streamflows, *Ecol. Appl.*, *4*(3), 544–554.

Barnes, H. H. (1967), *Roughness Characteristics of Natural Channels*, 213 pp., United States Government Printing Office, Washington, D. C.

Beauchamp, V. B., and J. C. Stromberg (2007), Flow regulation of the Verde River, Arizona encourages *Tamarix* recruitment but has minimal effect on *Populus* and *Salix* stand density, *Wetlands*, *27*(2), 381–389.

Bennett, S. J., T. Pirim, and B. D. Barkdoll (2002), Using simulated emergent vegetation to alter stream flow direction within a straight experimental channel, *Geomorphology*, *44*(1–2), 115–126.

Birkeland, G. H. (2002), Historical changes in flood power and riparian vegetation in lower Harris Wash, Escalante River Basin, Utah, *Phys. Geogr.*, *23*(1), 59–78.

Birken, A. S., and D. J. Cooper (2006), Processes of *Tamarix* invasion and floodplain development along the lower Green River, Utah, *Ecol. Appl.*, *16*(3), 1103–1120.

Brookes, C. J., J. M. Hooke, and J. Mant (2000), Modelling vegetation interactions with channel flow in river valleys of the Mediterranean region, *Catena*, *40*(1), 93–118.

Buffington, J. M., and D. R. Montgomery (1999), Effects of hydraulic roughness on surface textures of gravel-bed rivers, *Water Resour. Res.*, *35*(11), 3507–3521.

Cobby, D. M., D. C. Mason, and I. J. Davenport (2001), Image processing of airborne scanning laser altimetry data for improved river flood modelling, *ISPRS J. Photogramm.*, *56*(2), 121–138.

Cooper, D. J., D. C. Andersen, and R. A. Chimner (2003), Multiple pathways for woody plant establishment on floodplains at local to regional scales, *J. Ecol.*, *91*(2), 182–196.

Corenblit, D., E. Tabacchi, J. Steiger, and A. M. Gurnell (2007), Reciprocal interactions and adjustments between fluvial landforms and vegetation dynamics in river corridors: A review of complementary approaches, *Earth. Sci. Rev.*, *84*(1–2), 56–86.

Corenblit, D., J. Steiger, A. M. Gurnell, E. Tabacchi, and L. Roques (2009), Control of sediment dynamics by vegetation as a key function driving biogeomorphic succession within fluvial corridors, *Earth Surf. Process. Landf.*, *34*(13), 1790–1810.

Darby, S. E. (1999), Effect of riparian vegetation on flow resistance and flood potential, *J. Hydraul. Eng.-ASCE*, *125*(5), 443–454.

Dean, D. J., and J. C. Schmidt (2011), The role of feedback mechanisms in historic channel changes of the lower Rio Grande in the Big Bend region, *Geomorphology*, *126*(3–4), 333–349.

Elliott, J. G., and S. P. Anders (2004), Summary of sediment data from the Yampa River and Upper Green River Basins, Colorado and Utah, 1993–2002, *Scientific Investigations Report 2004–5242*. Division of Wildlife, U.S. Fish and Wildlife Service, U.S. Geological Survey, Denver, CO.

Everitt, B. (1993), Channel responses to declining flow on the Rio Grande between Ft. *Quitman and Presidio, Texas, Geomorphology*, *6*(3), 225–242.

Fathi-Maghadam, M., and N. Kouwen (1997), Nonrigid, nonsubmerged, vegetative roughness on floodplains, *J. Hydraul. Eng.-ASCE*, *123*(1), 51–57.

Fathi-Maghadam, M., K. Drikvandi, B. Lashkarara, and K. Hammadi (2011), Determination of friction factor for rivers with non-submerged vegetation in banks and floodplains, *Sci. Res. Essays*, *6*(22), 4714–4719.

Forzieri, G., L. Guarnieri, E. R. Vivoni, F. Castelli, and F. Preti (2011), Spectral-ALS data fusion for different roughness parameterizations of forested floodplains, *River Res. Appl.*, *27*(7), 826–840.

Forzieri, G., F. Castelli, and F. Preti (2012), Advances on remote sensing of hydraulic roughness, *Int. J. Remote Sens.*, *33*(2), 630–654.

Freeman, G. E., W. J. Rahmeyer, and R. R. Copeland (2000), Determination of resistance due to shrubs and woody vegetation, U.S. Army Engineer Research and Development Center, U.S. Army Corps of Engineers, Vicksburg, MS.

Friedman, J. M., G. T. Auble, P. B. Shafroth, M. L. Scott, M. F. Merigliano, M. D. Preehling, and E. K. Griffin (2005), Dominance of non-native riparian trees in western USA, *Biol. Invasions*, *7*(4), 747–751.

Gibson, C. A., J. L. Meyer, N. L. Poff, L. E. Hay, and A. Georgakakos (2005), Flow regime alterations under changing climate in two river basins: Implications for freshwater ecosystems, *River Res. Appl.*, *21*(8), 849–864.

Graf, W. L. (1978), Fluvial adjustments to the spread of tamarisk in Colorado Plateau region, *Geol. Soc. Am. Bull.*, *89*(10), 1491–1501.

Grams, P. E., and J. C. Schmidt (2002), Streamflow regulation and multilevel flood plain formation: Channel narrowing on the aggrading Green River in the eastern Unita Mountains, Colorado and Utah, *Geomorphology*, *44*(3–4), 337–360.

Griffin, E. R., and J. D. Smith (2004), Floodplain stabilization by woody riparian vegetation during an extreme flood, in *Riparian Vegetation and Fluvial Geomorphology*, edited by S. J. Bennett and A. Simon, pp. 221–236, AGU, Washington, D. C.

Griffin, E. R., J. W. Kean, K. R. Vincent, J. D. Smith, and J. M. Friedman (2005), Modeling effects of bank friction and woody bank vegetation on channel flow and boundary shear stress in the Rio Puerco, New Mexico, *J. Geophys. Res.*, *110*, F04023, doi:10.1029/2005JF000322.

Hereford, R. (1984), Climate and ephemeral-stream processes: Twentieth-century geomorphology and alluvial stratigraphy of the Little Colorado River, Arizona, *Geol. Soc. Am. Bull.*, *95*(6), 654–668.

Hodge, R., K. Richards, and J. Brasington (2007), A physically-based bedload transport model developed for 3-D reach-scale cellular modelling, *Geomorphology*, *90*(3–4), 244–262.

Hodge, R., J. Brasington, and K. Richards (2009), In situ characterization of grain-scale fluvial morphology using Terrestrial Laser Scanning, *Earth Surf. Process. Landf.*, *34*(7), 954–968.

Hygelund, B., and M. Manga (2003), Field measurements of drag coefficients for model large woody debris, *Geomorphology*, *51*(1–3), 175–185, doi: 10.1016/S0169-555X(02)00335-5.

James, C. S., A. L. Birkhead, A. A. Jordanova, and J. J. O'Sullivan (2004), Flow resistance of emergent vegetation, *J. Hydraul. Res.-ASCE*, *42*(4), 390–398.

Jarvela, J. (2002), Flow resistance of flexible and stiff vegetation: A flume study with natural plants, *J. Hydrol.*, *269*, 44–54.

Jarvela, J. (2004), Determination of flow resistance caused by non-submerged woody vegetation, *J. River Basin Manage.*, *2*(1), 61–70.

Kean, J. W., and J. Smith (2004), Flow and boundary shear stress in channels with woody bank vegetation, in *Riparian Vegetation and Fluvial Geomorphology*, edited by S. J. Bennett and A. Simon, pp. 237–252, AGU, Washington, D. C.

Kubrak, E., J. Kubrak, and P. M. Rowinski (2008), Vertical velocity distributions through and above submerged, flexible vegetation, *Hydrolog. Sci. J.*, *53*(4), 905–920.

Larson, G. (2004), *Tamarisk and Fluvial Geomorphic Form in Dinosaur National Monument, Colorado and Utah*, 129 pp., Utah State University, Logan, UT.

Liu, D., P. Diplas, J. D. Fairbanks, and C. C. Hodges (2008), An experimental study of flow through rigid vegetation, *J. Geophys. Res.*, *113*, F04015, doi: 10.1029/2008JF001042.

Logan, B. L. (2000), *Interactions Between Vegetation, Flow Dynamics, and Channel Change on the Colorado River, Colorado*, 134 pp., University of Colorado, Denver, Colorado.

MacArthur, R. H., and H. S. Horn (1969), Foliage profile by vertical measurements, *Ecology*, *50*, 802–804.

Manners, R. B., M. W. Doyle, and M. J. Small (2007), Structure and hydraulics of natural woody debris jams, *Water Resour. Res.*, *43*, W06432, doi: 10.1029/2006WR004910.

Manners, R. B., J. C. Schmidt, M. L. Scott, J. A. Scott, and C. M. U. Neale (2011), *Final report: investigate floodplain processes and riparian ecosystem linkages on the Yampa River and on the middle Green River in Dinosaur National Monument, Moffatt County, Colorado, and Uintah County, Utah, 25 pp.*, Colorado Plateau Cooperative Ecosystem Studies Unit, Dinasaur National Monument, National Park Service, Dinosaur, CO.

Mason, D. C., D. M. Cobby, M. S. Horritt, and P. D. Bates (2003), Floodplain friction parameterization in two-dimensional river flood models using vegetation heights derived from airborne scanning laser altimetry, *Hydrol. Process.*, *17*(9), 1711–1732.

Merritt, D. M., and E. E. Wohl (2006), Plant dispersal along rivers fragmented by dams, *River Res. Appl.*, *22*(1), 1–26.

Meyer, J. L., M. J. Sale, P. J. Mulholland, and N. L. Poff (1999), Impacts of climate change on aquatic ecosystem functioning and health, *J. Am. Water Resour. Assoc.*, *35*(6), 1373–1386.

Musleh, F. A., and J. F. Cruise (2006), Functional relationships of resistance in wide flood plains with rigid unsubmerged vegetation, *J. Hydraul. Eng.-ASCE*, *132*(2), 163–171.

Nepf, H. M. (1999), Drag, turbulence, and diffusion in flow through emergent vegetation, *Water Resour. Res.*, *35*(2), 479–489.

Nepf, H. M., J. A. Sullivan, and R. A. Zavistoski (1997), A model for diffusion within emergent vegetation, *Limnol. Oceanogr.*, *42*(8), 1735–1745.

Olden, J. D., N. L. Poff, and K. R. Bestgen (2006), Life-history strategies predict fish invasions and extirpations in the Colorado River Basin, *Ecol. Monogr.*, *76*(1), 25–40.

Petryk, S., and G. Bosmajian (1975), Analysis of flow through vegetation, *J. Hydraul. Eng.-ASCE*, *101*(7), 871–884.

Raupach, M. R. (1992), Drag and drag partition on rough surfaces, *Bound-Lay Meteorol.*, *60*(4), 375–395.

Rood, S. B., and J. M. Mahoney (1990), Collapse of riparian poplar forests downstream from dams in western prairies: Probable causes and prospects for mitigation, *Environ. Manage.*, *14*(4), 451–464.

Sandercock, P. J., and J. M. Hooke (2010), Assessment of vegetation effects on hydraulics and of feedbacks on plant survival and zonation in ephemeral channels, *Hydrol. Process.*, *24*(6), 695–713.

Schmidt, J. C., and D. M. Rubin (1995), Regulated streamflow, fine-grained deposits, and effective discharge in canyons with abundant debris fans, in *Natural and Anthropogenic Influences in Fluvial Geomorphology*, edited by J. E. Costa, A. J. Miller, K. W. Potter, and P. R. Wilcock, pp. 177–195, AGU, Washington, D. C.

Schnauder, I., and H. Moggridge (2009), Vegetation and hydraulic-morphological interactions at the individual plant, patch and channel scale, *Aquat. Sci.*, *71*(3), 318–330.

Shields, F. D., and C. J. Gippel (1995), Prediction of effects of woody debris removal on flow resistance, *J. Hydraul. Eng.-ASCE*, *121*(4), 341–354.

Smith, J. D. (2004), The role of riparian shrubs in preventing floodplain unraveling along the Clark Fork of the Columbia River in the Deer Lodge Valley, Montana, in *Riparian Vegetation and Fluvial Geomorphology*, edited by S. J. Bennett and A. Simon, pp. 71–85, AGU, Washington, D. C.

Steffler, P., and J. Blackburn (2002), *River2D: Two-Dimensional Depth Averaged Model of River Hydrodynamics and Fish Habitat, Introduction to Depth Averaged Modeling and User's Manual*, 120 pp., University of Alberta, Alberta, Canada.

Stephan, U., and D. Gutknecht (2002), Hydraulic resistance of submerged flexible vegetation, *J. Hydrol.*, *269*(1–2), 27–43.

Stoesser, T., C. A. M. E. Wilson, P. D. Bates, and A. Dittrich (2003), Application of a 3D numerical model to a river with vegetated floodplains, *J. Hydroinform.*, *5*, 99–112.

Stone, B. M., and H. T. Shen (2002), Hydraulic resistance of flow in channels with cylindrical roughness, *J. Hydraul. Eng.-ASCE*, *128*(5), 500–506.

Straatsma, M. W., J. J. Warmink, and H. Middelkoop (2008), Two novel methods for field measurements of hydrodynamic density of floodplain vegetation using terrestrial laser scanning and digital parallel photography, *Int. J. Remote Sens.*, *29*(5), 1595–1617.

Stromberg, J. C., B. D. Richter, D. T. Patten, and L. G. Wolden (1993), Response of a Sonoran riparian forest to a 10-year return flood, *Great Basin Nat.*, *53*(2), 118–130.

Tal, M., and C. Paola (2007), Dynamic single-thread channels maintained by the interaction of flow and vegetation, *Geology*, *35*(4), 347–350.

Thies, M., N. Pfeifer, D. Winterhalder, and B. G. H. Gorte (2004), Three-dimensional reconstruction of stems for assessment of taper, sweep and lean based on laser scanning of standing trees, *Scand. J. Forest Res.*, *19*(6), 571–581.

Todd, K. W., F. Csillag, and P. M. Atkinson (2003), Three-dimensional mapping of light transmittance and foliage distribution using lidar, *Can. J. Remote Sens.*, *29*(5), 544–555.

Turner, R. M., and M. M. Karpiscak (1980), Recent vegetation changes along the Colorado River between Glen Canyon Dam and Lake Mead, Arizona, *U.S. Geological Survey, Professional Paper*, *1132*, pp. 1–125, U. S. Geological Survey, Denver, CO.

Velasco, D., A. Bateman, and V. Medina (2008), A new integrated, hydro-mechanical model applied to flexible vegetation in riverbeds, *J. Hydraul. Res.*, *46*(5), 579–597.

Warmink, J. J. (2007), *Vegetation Density Measurements using Parallel Photography and Terrestrial Laser Scanning*, 83 pp., Utrecht University, Utrecht, The Netherlands.

Webb, R. H., S. A. Leake, and R. M. Turner (2007), *The Ribbon of Green: Change in Riparian Vegetation in the Southwestern United States*, 480 pp., The University of Arizona Press, Tucson, AZ.

Whiting, P. J., and W. E. Dietrich (1990), Boundary shear-stress and roughness over mobile alluvial beds, *J. Hydraul. Eng.-ASCE*, *116*(12), 1495–1511.

Zhang, K. Q., S. C. Chen, D. Whitman, M. L. Shyu, J. H. Yan, and C. C. Zhang (2003), A progressive morphological filter for removing nonground measurements from airborne LIDAR data, *IEEE T. Geosci. Remote*, *41*(4), 872–882.

Zong, L. J., and H. Nepf (2010), Flow and deposition in and around a finite patch of vegetation, *Geomorphology*, *116*(3–4), 363–372.